Frictional cohesive zone model for quasi-brittle fracture: mixed-mode and coupling between cohesive and frictional behaviors

Vincent Venzal, Stéphane Morel, Thomas Parent, Frédéric Dubois

Frictional Cohesive Zone Model for quasi-brittle fracture: Mixed-mode and coupling between cohesive and frictional behaviors

V. Venzal[a,c], S. Morel[a,*], T. Parent[a], F. Dubois[b]

[a] *Université de Bordeaux, UMR5295, Institut de Mécanique et d'Ingénierie-Bordeaux (I2M), Dépt. Génie Civil et Environnemental (GCE), Bordeaux F-33000, France*
[b] *LMGC, Univ Montpellier, CNRS, Montpellier, France*
[c] *AIA Ingénierie, 10 rue Ariane, Bât C, 33700 Mérignac, France*

Abstract

In this study, a general frictional cohesive zone model (FCZM) dedicated to quasi-brittle fracture is proposed to describe the mechanical response of an interface under combined traction or compression and shear loadings. Under combined traction and shear loadings, mixed-mode $I + II$ cohesive zone model, as proposed by Camanho et al. (2003), is used to express the mixed-mode response of the interface and the dependence to the loading path consistent to the one expected in quasi-brittle fracture. Under combined compression and shear loadings, the novelty lies in the proposed coupling between Mode II cohesive behavior and frictional behavior based on the damage level leading to a progressive rising of the frictional stress associated with the softening part of the cohesive behavior of the interface. FCZM thus describes a smooth transition from a cohesive zone to a pure frictional contact zone. Applied to the masonry context, this general FCZM can be fully characterized through two fracture tests carried out on small masonry assemblages. Finally, FCZM is implemented in LMGC90 discrete element code and used to simulate the experimental response of an unilateral cyclic shear test carried out on a triplet of limestone blocks assembled by two mortar joints.

Keywords: Quasi-brittle fracture, Cohesive zone model, Mixed-mode, Frictional behavior, Discrete Element Method, Masonry assemblages

*stephane.morel@u-bordeaux.fr

1. Introduction

The basic hypothesis of cohesive zone models is that failure can be described through a fictitious surface crack (which is usually characterized by a zero thickness interface) which transmits normal and shear stresses. The magnitudes of normal and shear stresses are described from functions (monotonically decreasing) of the opening displacement (Mode I) and of the shear plane displacement (Mode II) of the interface.

In literature there is a large variety of Cohesive Zone Models (CZM) which can be differentiated according to the shape of their softening parts: rigid-linear (Camacho and Ortiz, 1996; Snozzi and Molinari, 2013), bi-linear (Hilleborg et al., 1976; Camanho et al., 2003; Högberg, 2006), tri-linear (Morel et al., 2010; Bisoffi-Sauve et al., 2019) and exponential CZM (Xu and Needleman, 1993; van den Bosch et al., 2006). In those models, the cohesive stresses decrease (after an elastic domain) according to the rising of a damage variable (scalar) usually noted as d. Mode I and Mode II cohesive behaviors are generally described according to softening functions exhibiting a similar shape.

In the case of combined traction and shear loadings, Mode I and Mode II cohesive behaviors can be coupled or uncoupled. Uncoupled CZM are typically used when interface separation occurs in a single predefined direction, while coupled CZM are used for complex loading leading simultaneously to opening and shear plane displacements of the interface. Coupled CZM generally differ according to the criteria used to describe the mixed-mode $I+II$ failure and the dependence (or not) to the loading path exhibited by the material fracture (van den Bosch et al., 2006; Camanho et al., 2003; Dimitri et al., 2015).

In the case of combined compression and shear loadings, the contribution of the friction phenomenon complicates the analysis of the respective contributions of the frictional and cohesive behaviors in the mechanical response of the interface. As such, if the cohesive behavior is estimated by simply subtracting the value of the *full* friction stress from the total shear stress-shear plane displacement response (Freddi et al., 2017; Baek and Park, 2018; Bisoffi-Sauve et al., 2019; Yuen et al., 2019), the resulting Mode II cohesive energy is usually underestimated and associated with a physically inconsistent dependence to the normal stress. Note that such an assumption of

superimposition of *full* friction stress and cohesive stress leads to consider that the cohesive behavior is only activated if the full friction threshold is reached or, in other words, that the friction effect takes place while the cohesive capacity of interface is still intact, which appears to be physically inconsistent. To overcome this issue, several authors (Chaboche et al., 1997; Snozzi and Molinari, 2013; Spring and Paulino, 2015; D'Altri et al, 2018) have proposed phenomenological evolutions of the friction stress as a function of the shear plane displacement superimposed to the cohesive behavior. Nevertheless, even if these *frictional* cohesive zone models allow a better description of experimental stress-displacement responses, assuming a friction stress function of the shear plane displacement is not physically based since frictional effect is expected to depend only on the normal stress, the friction coefficient and the area of the surface on which it acts. A coupling based on the damage part of the interface on which the frictional phenomenon can physically act appears more relevant (Raous and Monerie, 2002; Acary and Monerie, 2006; Alfano and Sacco, 2006).

On this basis, we propose a general Frictional Cohesive Zone Model dedicated to quasi-brittle fracture describing the mechanical response of an interface under combined traction or compression and shear loadings. In Section 2, the cohesive laws with exponential softening used for pure Mode I and Mode II fractures are presented and a reminder of the physical meaning of the damage variable driving the softening part is proposed. On this basis, under combined traction and shear loadings (Section 3), mixed-mode $I + II$ cohesive zone model proposed by Camanho et al. (2003) is used to express the mixed-mode response of the interface and the dependence to the loading path consistent to the one expected in quasi-brittle fracture. Under combined compression and shear loadings (Section 4), the novelty lies in the proposed coupling between cohesive and frictional behaviors which is obtained through an estimate of the effective frictional area, itself estimated from the damage variable. A first illustration of the response obtained from FCZM under cyclic shear loading is proposed. In Section 5, the FCZM is used in the context of masonry and two characterization tests allowing the estimation of all the cohesive and frictional parameters of a block-mortar interface are described. The methodology used to estimate simultaneously the frictional and Mode II cohesive parameters is particularly discussed. Finally, in Section 6, the FCZM is implemented in LMGC90 discrete element code and used to simulate the experimental response of an unilateral cyclic shear test carried out on a triplet of limestone blocks assembled by two mortar joints.

2. Cohesive law with exponential softening

The accurate simulation of interfacial failure in quasi-brittle materials needs to use an appropriate cohesive law allowing in particular the description of (i) the negative hardening expected for the tension and shear stress-displacement responses of the interface, (ii) the dependence on the loading path and of (iii) the strong dissymmetry of tensile and shear fracture properties.

Among the different functions used to describe the softening behavior in CZM, exponential softening allows fitting, with a reasonable accuracy, of the negative and concave hardening function expected in quasi-brittle fracture as shown in Figure 1. In this study, one proposes to describe the Mode I and Mode II cohesive behaviors from the same shape of cohesive law (exponential softening) as shown in Figure 1 where $i = \{I, II\}$. The initial elastic behavior is characterized by the stiffness K_i^0 [N/m^3] and the tensile ($i = I$) or shear ($i = II$) strength σ_i^e [N/m^2]. The stress σ_i as well as the stiffness K_i decrease continuously reflecting the softening behavior of the interface (Fig. 1). The decrease of the stiffness K_i from its initial value K_i^0 (and

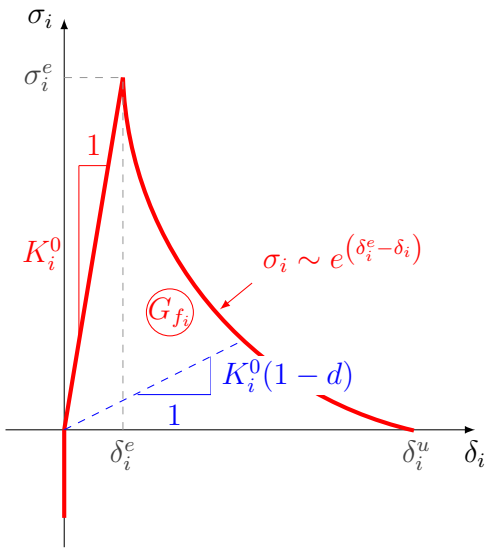

Figure 1: Cohesive law with exponential softening

consequently, the one of the cohesive stress σ_i from the strength σ_i^e) is driven by a damage variable d (scalar variable). The damage variable d reflects the

level of the mechanical degradation of the interface which can be described through the development of crack surface. In this way and particularly in Mode I, d is defined as the ratio of the cracked surface A_d [m^2] over the whole interfacial surface area A_0 [m^2], *i.e.,* $d = A_d/A_0$. Thus $0 \leq d \leq 1$, $d = 0$ corresponding to an intact interface ($A_d = 0$) while $d = 1$ reflects the overall failure of the interface ($A_d = A_0$). Thus, for a given damage level d, the load F_i transmitted by the interface can be expressed either with the *apparent* stress σ_i applied on the whole interface surface A_0 or with the *effective* stress $\tilde{\sigma}_i$ applied on the healthy surface of the interface $\tilde{A}$:

$$F_i = \tilde{\sigma}_i \tilde{A} = \sigma_i A_0, \tag{1}$$

where the healthy surface $\tilde{A}$ can be related to the whole surface A_0 and the damage surface A_d as:

$$\tilde{A} = A_0 - A_d = A_0(1 - d) \tag{2}$$

Thus, from Equations (1) and (2), the apparent cohesive stress σ_i can be expressed as a function of the effective one $\tilde{\sigma}_i$ as:

$$\sigma_i = (1 - d)\tilde{\sigma}_i \tag{3}$$

Anyway, the displacement δ_i is the same for the apparent and effective behaviors of the interface, such as:

$$\delta_i = \frac{\sigma_i}{K_i} = \frac{\tilde{\sigma}_i}{K_i^0}, \tag{4}$$

Thus, introducing Eq.(4) into Eq.(3) leads to the expression of the apparent stiffness [1]:

$$K_i = (1 - d)K_i^0, \tag{5}$$

hence, the apparent cohesive stress yields:

$$\sigma_i = K_i^0(1 - d)\delta_i \tag{6}$$

[1] In case of zero thickness interface, the initial stiffness K_i^0 must tend towards infinity if the adhesion at the interface is perfect (K_i^0 is then qualified as a *penalty* stiffness) while K_i^0 will take a finite value in the case of a lack of cohesion of the interface which can be described from an initial damage surface A_d or, in a equivalent way, from an initial value of the damage variable d according to Eq.(5).

as shown in Figure 1.
According to Eq.(6), the softening behavior of the interface is related to the increase of the damage variable d while the apparent stress σ_i follow an exponential function:

$$\sigma_i(\delta_i) = \sigma_i^e e^{\phi_i(\delta_i^e - \delta_i)}, \tag{7}$$

where $\delta_i^e = \sigma_i^e / K_i^0$ [m] corresponds to the displacement at the end of the elastic regime and such as the cohesive energy G_{f_i} [J/m^2] verify $G_{f_i} = \int_0^\infty \sigma_i \, \mathrm{d}\delta_i$ which leads to:

$$\phi_i = \frac{2K_i^0 \sigma_i^e}{2K_i^0 G_{f_i} - (\sigma_i^e)^2} \tag{8}$$

According to Equations (6) and (7), the damage variable d can be expressed as:

$$d = 1 - \frac{\sigma_i^e}{K_i^0 \delta_i} e^{\phi_i \left(\frac{\sigma_i^e}{K_i^0} - \delta_i \right)} \tag{9}$$

Note that, according to the second law of the thermodynamics of irreversible processes, the evolution of the damage parameter is always positive ($\dot{d} \geq 0$, $d = max(d_{history})$).

To resume, for each fracture mode ($i = I$: Mode I and $i = II$: Mode II), the cohesive law of the interface is described with only three cohesive parameters: the initial stiffness K_i^0, the tensile or shear strength σ_i^e and the cohesive energy G_{f_i}. Thus, the pure Mode i cohesive law can be summarized as:

$$\sigma_i(\delta_i) = \begin{cases} K_i^0 \delta_i & \text{if } \delta_i \leq \delta_i^e \\ \sigma_i^e e^{\phi_i(\delta_i^e - \delta_i)} & \text{if } \delta_i^e \leq \delta_i < \delta_i^u \\ 0 & \text{if } \delta_i \geq \delta_i^u \end{cases} \tag{10}$$

where ϕ_i has been previously defined from Eq.(8) and δ_i^u corresponds to an upper cut-off of the displacement which can be introduced in order to indicate artificially the total failure of the interface (*i.e.*, $\sigma_i = 0$ and $d = 1$ for $\delta_i \geq \delta_I^u$) because the exponential function defined in Eq.(7) tends to $\sigma_i = 0$ asymptotically as a function of displacement δ_i. For instance, the upper cut-off of the displacement δ_i^u can be estimated from a percentage η of the strength σ_i^e that leads, in the case of an exponential softening, to:

$$\delta_i^u = \delta_i^e - \frac{1}{\phi_i} \ln(\eta) \tag{11}$$

3. Combined traction and shear loading: mixed-mode I+II CZM

3.1. Mixed-mode $I + II$

First CZMs (Hilleborg et al., 1976; Xu and Needleman, 1993; Camacho and Ortiz, 1996) have been developed for single mode fracture processes (*i.e.* for pure Mode I or pure Mode II fractures). Nevertheless, an interface is generally loaded in Mode I and in Mode II simultaneously (Zucchini and Lourenço, 2002) leading to *mixed-mode* $I + II$ fracture process. Therefore, various mixed-mode $I + II$ cohesive zone models have been proposed in order to describe such a complex fracture process (van den Bosch et al., 2006; Högberg, 2006; Snozzi and Molinari, 2013; Bisoffi-Sauve et al., 2019) which are mostly inspired by the pioneering model due to Camanho et al. (2003). The mixed-mode $I + II$ CZM proposed by Camanho et al. (2003) is formulated from the pure modes (Mode I and Mode II) cohesive laws (as detailed in the preceding Section) and leads to the expression of a mixed-mode cohesive law which has a form similar to those used for pure modes (Fig. 1), *i.e.*, characterized by an initial stiffness K^0_{I+II}, a strength σ^e_{I+II} (or a limit elastic displacement δ^e_{I+II}) and a cohesive energy $G_{f_{I+II}}$ as shown in Figure 2.
The mix of modes is obtained on the basis of a coupling parameter β corresponding to the ratio of the shear plane component of the displacement $\delta_{II_{I+II}}$ over the normal one $\delta_{I_{I+II}}$:

$$\beta = \frac{\delta_{II_{I+II}}}{\delta_{I_{I+II}}} = \tan(\alpha), \tag{12}$$

and from two criteria, the first one relating to the damage initiation and the second one corresponding to the interface failure.

Damage initiation criterion. It is assumed that the mixed-mode limit elastic stress σ^e_{I+II} corresponding to the damage onset and especially its Mode I and Mode II components, respectively noted as $\sigma^e_{I_{I+II}}$ and $\sigma^e_{II_{I+II}}$, must satisfy the quadratic stress criterion:

$$\left(\frac{\sigma^e_{I_{I+II}}}{\sigma^e_I}\right)^2 + \left(\frac{\sigma^e_{II_{I+II}}}{\sigma^e_{II}}\right)^2 = 1, \tag{13}$$

where, σ^e_I corresponds to the tensile strength in pure Mode I and σ^e_{II} is the shear strength in pure Mode II previously defined in Section 2.
On this basis, the initial stiffness of the Mode I and Mode II components

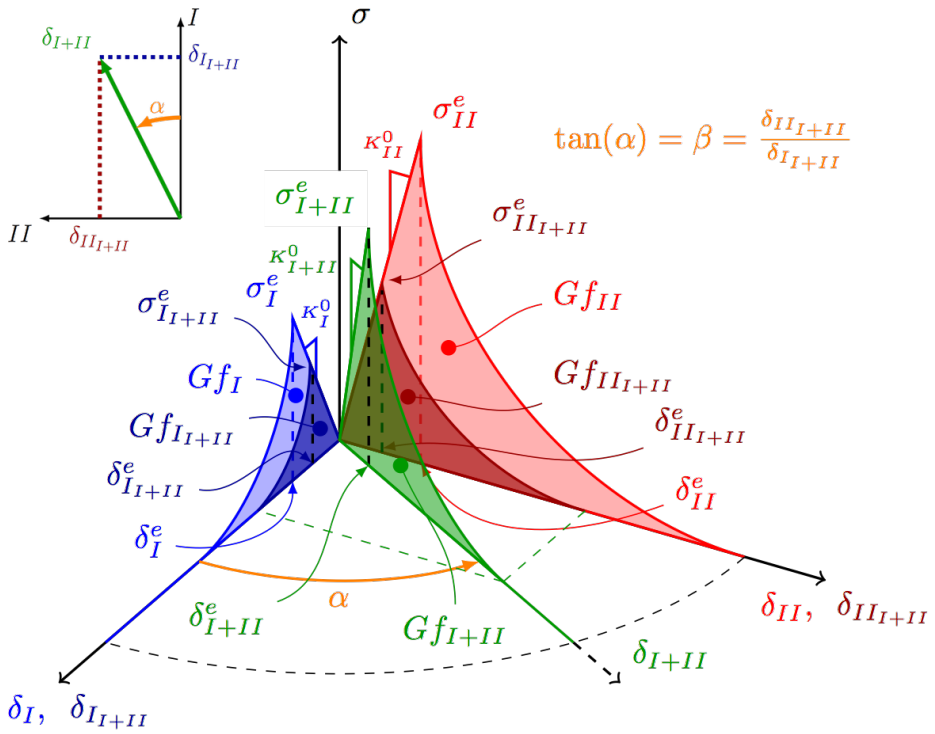

Figure 2: Mixed-mode cohesive law

of the mixed-mode being equal to the initial stiffness of the pure modes, *i.e.* $K^0_{I_{I+II}} = K^0_I$ and $K^0_{II_{I+II}} = K^0_{II}$, the quadratic stress criterion [Eq.(13)] can be rewritten in terms of displacements as:

$$\left(\frac{\delta^e_{I_{I+II}}}{\delta^e_I}\right)^2 + \left(\frac{\delta^e_{II_{I+II}}}{\delta^e_{II}}\right)^2 = 1 \tag{14}$$

Thus, using the relationships between the displacement δ_{I+II}, its Mode I and Mode II components ($\delta^e_{I_{I+II}}$ and $\delta^e_{II_{I+II}}$ respectively) and the coupling parameter β [Eq.(12)], the mixed-mode limit elastic displacement δ^e_{I+II} can be obtained from Equation (14) such as:

$$\delta^e_{I+II} = \delta^e_I\,\delta^e_{II}\sqrt{\frac{1+\beta^2}{(\delta^e_{II})^2 + (\delta^e_I\beta)^2}} \tag{15}$$

where δ^e_I and δ^e_{II} are the limit elastic displacements of the pure modes I and

II respectively [Eq.(10)]. Note that, according to Equation (15), a Mode I loading corresponding to a value of the coupling parameter $\beta = 0$ leads to $\delta^e_{I+II} = \delta^e_I$ while a Mode II loading, inducing $\beta \to \infty$, leads to $\delta^e_{I+II} = \delta^e_{II}$. Finally, the expression of the mixed-mode $I + II$ limit elastic stress σ^e_{I+II} yields:

$$\sigma^e_{I+II} = \delta^e_I \delta^e_{II} \sqrt{\frac{K_I^{0^2} + \beta^2 K_{II}^{0^2}}{\delta^{e^2}_{II} + \beta^2 \delta^{e^2}_I}} \tag{16}$$

Note that pure Mode I loading and pure Mode II loading correspond also to particular cases of Equation (16) insofar as $\sigma^e_{I+II} = \sigma^e_I$ for $\beta = 0$ and $\sigma^e_{I+II} = \sigma^e_{II}$ for $\beta \to \infty$ (Figure 3).

Failure criterion. The failure of an interface under mixed-mode loading is governed by the mixed-mode cohesive energy $G_{f_{I+II}}$. This cohesive energy can be expressed from the sum of its Mode I and Mode II components, $G_{f_{I_{I+II}}}$ and $G_{f_{II_{I+II}}}$ respectively, such as:

$$G_{f_{I+II}} = G_{f_{I_{I+II}}} + G_{f_{II_{I+II}}} \tag{17}$$

On this basis, a second criterion, named as *failure criterion* is necessary to estimate the value of mixed-mode cohesive energy $G_{f_{I+II}}$ (van den Bosch et al., 2006; Högberg, 2006; Snozzi and Molinari, 2013; Bisoffi-Sauve et al., 2019). This failure criterion is usually expressed through a power law of the Mode I and Mode II components of the cohesive energy, such as:

$$\left(\frac{G_{f_{I_{I+II}}}}{G_{f_I}}\right)^n + \left(\frac{G_{f_{II_{I+II}}}}{G_{f_{II}}}\right)^m = 1 \tag{18}$$

where G_{f_I} and $G_{f_{II}}$ are the cohesive energies relative to the pure modes I and II respectively (Section 2).
As a first approximation, a linear relationship is usually chosen from Eq.(18), *i.e.* $n = m = 1$ (Bisoffi-Sauve et al., 2019). Such a linear relationship ($n = m = 1$) will be also assumed in this study.
Let us express the Mode I and Mode II components of the mixed-mode cohesive energy as:

$$G_{f_{I_{I+II}}} = \Psi_{I_{I+II}}\, G_{f_I} \tag{19}$$

$$G_{f_{II_{I+II}}} = \Psi_{II_{I+II}}\, G_{f_{II}} \tag{20}$$

where $\Psi_{I_{I+II}}$ [1] and $\Psi_{II_{I+II}}$ [1] correspond respectively to the fractions of the *pure* Mode I and Mode II cohesive energies in the correspondent components of the mixed-mode cohesive energy. Therefore, according to Equations (19) and (20), the failure criterion defined in Eq.(18) yields :

$$\Psi_{I_{I+II}} + \Psi_{II_{I+II}} = 1 \tag{21}$$

Moreover, a given cohesive energy G_{f_i} can be expressed as the sum of the energy associated with the elastic part $G_{f_i}^e = \sigma_i^e \delta_i^e / 2$ and the one related to the softening part $G_{f_i}^{soft}$, i.e., $G_{f_i} = G_{f_i}^e + G_{f_i}^{soft}$. On this basis, the ratio of the *elastic* energy over the whole cohesive energy energy of a given mode must be maintained in the corresponding component of the mixed-mode such as:

$$\frac{G_{f_I}^e}{G_{f_I}} = \frac{G_{f_{I_{I+II}}}^e}{G_{f_{I_{I+II}}}} = {\phi_I}^e = cte \tag{22}$$

$$\frac{G_{f_{II}}^e}{G_{f_{II}}} = \frac{G_{f_{II_{I+II}}}^e}{G_{f_{II_{I+II}}}} = {\phi_{II}}^e = cte \tag{23}$$

Note that such ratio could be also expressed from the softening part of the cohesive behaviors. Finally, the parameters describing the elastic part of the cohesive behavior in pure modes (Section 2) and those of the mixed-mode (obtained from the damage initiation criterion) being known, the fraction of the Mode I cohesive energy in the mixed-mode cohesive energy $\Psi_{I_{I+II}}$ can be expressed, according to Equations (19) and (22), as:

$$\Psi_{I_{I+II}} = \frac{G_{f_{I_{I+II}}}}{G_{f_I}} = \frac{G_{f_{I_{I+II}}}^e}{G_{f_I}^e} = \frac{{\delta_{II}^e}^2}{{\delta_{II}^e}^2 + \beta^2 {\delta_I^e}^2} \tag{24}$$

while, according to Equations (20) and (23), the fraction of the Mode II cohesive energy in the mixed-mode cohesive energy $\Psi_{II_{I+II}}$ yields:

$$\Psi_{II_{I+II}} = \frac{G_{f_{II_{I+II}}}}{G_{f_{II}}} = \frac{G_{f_{II_{I+II}}}^e}{G_{f_{II}}^e} = \frac{\beta^2 {\delta_I^e}^2}{{\delta_{II}^e}^2 + \beta^2 {\delta_I^e}^2} \tag{25}$$

Note that, according to Equations (24) and (25), a Mode I loading corresponding to a value of the coupling parameter $\beta = 0$ leads to fractions of the Mode I and Mode II cohesive energies such as $\Psi_{I_{I+II}} = 1$ and $\Psi_{II_{I+II}} = 0$ and

hence, according to Equations (17) and (19), the mixed-mode cohesive energy is then equal to the Mode I cohesive energy $G_{f_{I+II}} = G_{f_I}$ as expected intuitively. Conversely, a Mode II loading inducing a coupling parameter $\beta \to \infty$ leads to fractions of the Mode I and Mode II cohesive energies such as $\Psi_{I_{I+II}} = 0$ and $\Psi_{II_{I+II}} = 1$ and so, according to Equations (17) and (20), to mixed-mode cohesive energy $G_{f_{I+II}} = G_{f_{II}}$, *i.e.*, the Mode II cohesive energy.

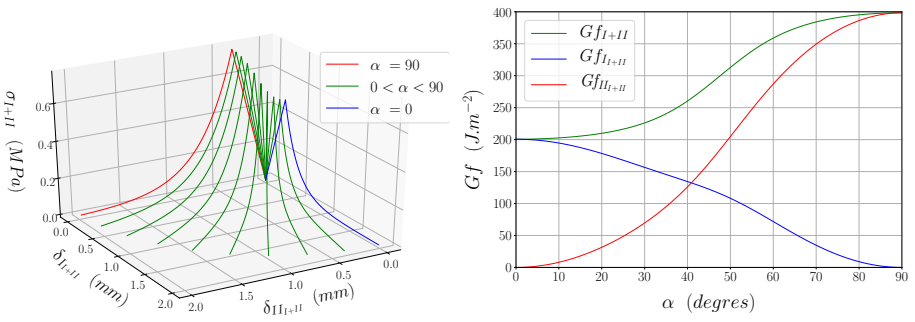

(a) (b)

Figure 3: Mixed-mode CZM as a function of the α angle: (a) Cohesive behavior *vs* α and (b) Mixed-mode cohesive energy and its Mode I and Mode II components *vs* α obtained for $G_{f_I} = 200J/m^2$ and $G_{f_{II}} = 400J/m^2$.

Figure 3(a) exhibits the response of the mixed-mode CZM when the interface is subjected to a monotonically rising displacement δ_{I+II} up to the ultimate displacement δ^u_{I+II} according to various α angles (Fig. 2) ranged between 0 and 90 degrees. It can be observed from Figure 3(b) that mixed-mode cohesive energy $G_{f_{I+II}}$ (Equation 17) increases from the Mode I cohesive energy $G_{f_{I+II}} = G_{f_{I_{I+II}}} = G_{f_I}$ when the interface is loaded according to $\alpha = 0\,\text{deg}$ (for this example, the value G_{f_I} has been fixed to $200J/m^2$) to the Mode II cohesive energy when $\alpha = 90\,\text{deg}$, i.e., $G_{f_{I+II}} = G_{f_{II_{I+II}}} = G_{f_{II}}$ with here $G_{f_{II}} = 400J/m^2$.

3.2. Influence of the mixed-mode coupling on the dissipated energy

As previously mentioned, the quasi-brittle damage being caused by extension, the dissipated energy is expected to be different if the interface is firstly loaded in pure traction then in pure shear and conversely. A way of studying the behavior of a coupled cohesive zone law is to analyze the dissipated energy under combined normal and shear loading as proposed by van

den Bosch et al. (2006).
In a first case, the interface is loaded in the direction I (*i.e.*, $\alpha = 0\,\text{deg}$) up to a displacement $\delta^*_{I_{I+II}}$ whose value is a percentage of the ultimate one δ^u_I then, $\delta^*_{I_{I+II}}$ is kept constant and a displacement is applied in the direction II up to the corresponding ultimate one $\delta_{II_{I+II}} = \delta^u_{II}$ (Fig. 4(a)). This first case of non-proportional loading is applied for various ratio $\delta^*_{I_{I+II}}/\delta^u_I$ ranged between 0 and 1.
In the second case (Fig. 4(b)), the interface is firstly loaded in the direction II (*i.e.*, $\alpha = 90\,\text{deg}$) up to a displacement $\delta^*_{II_{I+II}}$ corresponding to a percentage of the ultimate one δ^u_{II} then, $\delta^*_{II_{I+II}}$ is kept constant and a displacement is applied in the direction I up to the ultimate one $\delta_{I_{I+II}} = \delta^u_I$. As for the first case, the second loading case is applied for various ratio $0 \leq \delta^*_{II_{I+II}}/\delta^u_{II} \leq 1$.
The mixed-mode energy $G_{f_{I+II}}$ dissipated during both cases as well as the

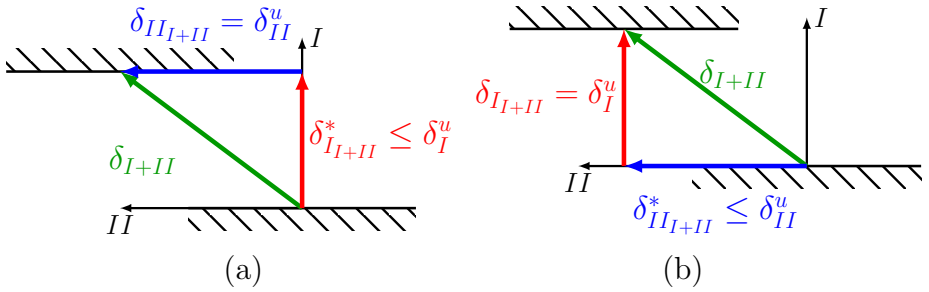

Figure 4: Loading sequence to study the influence of the coupling parameters on the work-of-separation: as proposed by van den Bosch et al. (2006)

Mode I and Mode II components of this energy, $G_{f_{I_{I+II}}}$ and $G_{f_{II_{I+II}}}$ respectively, are plotted in Figure 5 as a function of the ratio $\delta^*_{I_{I+II}}/\delta^u_I$ relative to the first case (Fig. 5(a)) and $\delta^*_{II_{I+II}}/\delta^u_{II}$ corresponding to the second case (Fig. 5(b)).
In the first case (Fig. 5(a)), as expected, the dissipated energy $G_{f_{I+II}} = G_{f_{II_{I+II}}} = G_{f_{II}}$ when the ratio $\delta^*_{I_{I+II}}/\delta^u_I = 0$ which corresponds to a pure shear loading of the interface while, $G_{f_{I+II}} = G_{f_{I_{I+II}}} = G_{f_I}$ when $\delta^*_{I_{I+II}}/\delta^u_I = 1$ corresponding to pure traction loading. Moreover, the dissipated energy decreases monotonically as a function of the ratio $\delta^*_{I_{I+II}}/\delta^u_I$ from $G_{f_{II}}$ to G_{f_I} exhibiting a consistent physical behavior.
In the second case (Fig. 5(b)), the dissipated energy $G_{f_{I+II}}$ increases monotonically as a function of the ratio $\delta^*_{II_{I+II}}/\delta^u_{II}$ from $G_{f_{I+II}} = G_{f_{I_{I+II}}} = G_{f_I}$ when $\delta^*_{II_{I+II}}/\delta^u_{II} = 0$ which corresponds to pure traction loading of the inter-

face, to $G_{f_{I+II}} = G_{f_{II_{I+II}}} = G_{f_{II}}$ when $\delta^*_{II_{I+II}}/\delta^u_{II} = 1$ corresponding a pure shear loading of the interface.
As a conclusion, the monotonous evolutions of the mixed-mode dissipated energy observed from both loading cases in Figures 5(a) and 5(b) seems to be consistent with the expected behavior of a quasi-brittle interface.

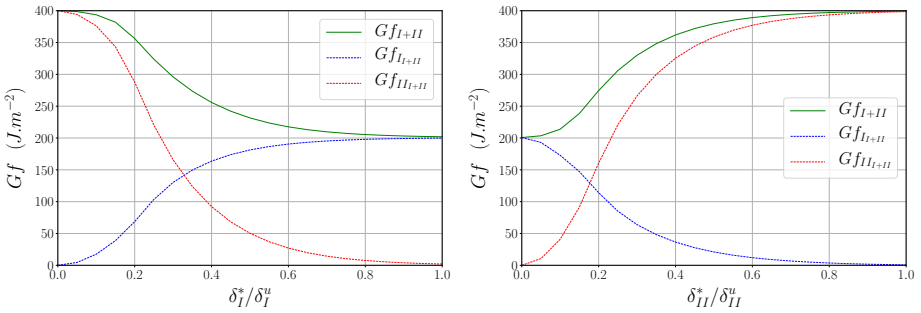

(a) (b)

Figure 5: Energy dissipated from non proportionnal loading (with $Gf_I = 200J/m^2$ and $Gf_{II} = 400J/m^2$)

In the following part, cases of combined compression and shear loadings applied to the interface are studied. In these cases, friction effect strongly influences the mechanical response of the interface and hence, a coupling between frictional and Mode II cohesive behaviors based on an estimation of the effective frictional area is proposed.

4. Combined compression and shear loading: Frictional Mode II CZM

4.1. Monotonically loading

When the interface is subjected to shear and compression loading, the contribution of the friction must be taken into account to describe accurately the interface behavior. As mentioned in Introduction, in most models, the *full* friction stress is usually considered from the onset of cohesive behavior and leads to consider that the friction effect takes place while the cohesive capacity of the interface is still intact. To overcome this physical inconsistency, several authors (Chaboche et al., 1997; Snozzi and Molinari, 2013; Spring and Paulino, 2015; D'Altri et al, 2018) introduce, in their CZM, a phenomenological progressive rising of the friction stress as a function of

the shear plane displacement which allow a better description of experimental stress-displacement responses. Nevertheless, assuming a friction stress depending of shear plane displacement is not physically based because friction stress is expected to depend only on normal stress, on friction coefficient and on the surface area on which acts the friction effect. Thus, as proposed by Raous and Monerie (2002), Acary and Monerie (2006) and Alfano and Sacco (2006), a coupling based on the damage part of the interface on which the frictional phenomenon can physically act appears more relevant.
In the following, taking inspiration from these latter works, a frictional Mode II cohesive zone model founded on a physically based coupling of cohesive and frictional behaviors is proposed. The coupling is here introduced from the damage variable, single internal variable of the model, which gives an estimate of the effective damage area of the interface.

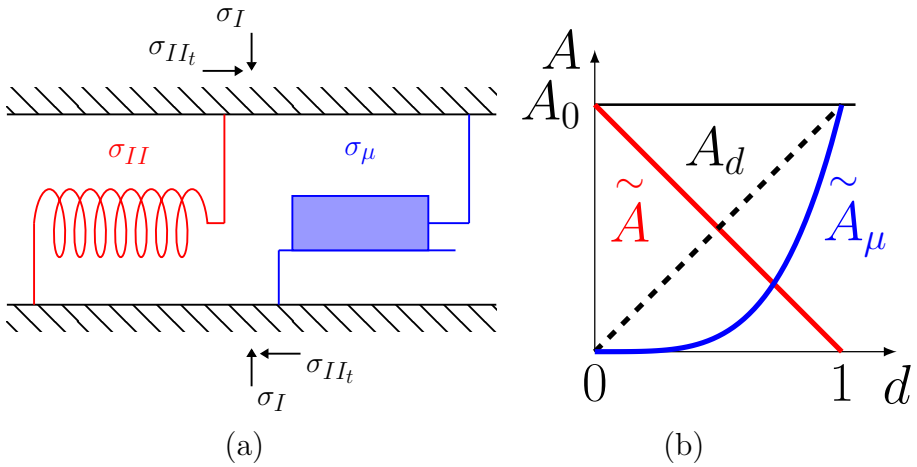

Figure 6: Combined compression and shear loading, based on apparent stresses: (a) rheological model, and on effective stresses: (b) evolution of effective areas against interface area A_0

Let us consider the rheological model shown in Figure 6(a) which consists in a cohesive spring and a friction pad in parallel in order to describe the interface mechanical behavior. According to this rheological model, the shear stress σ_{II_t} can be expressed as the sum of the cohesive stress σ_{II} and the frictional stress σ_μ:

$$\sigma_{II_t} = \sigma_{II} + \sigma_\mu \tag{26}$$

Note that all stresses in Eq.(26) correspond to *apparent* stresses, *i.e.*, stresses

acting on the whole surface of the interface A_0.
Moreover, according to Eq.(1), the apparent cohesive stress σ_{II} [Eq.(26)] can be expressed from the effective cohesive stress $\tilde{\sigma}_{II}$ acting on the effective cohesive area $\tilde{A} = A_0(1-d)$ and yields:

$$\sigma_{II} = \tilde{\sigma}_{II}\frac{\tilde{A}}{A_0} = \tilde{\sigma}_{II}(1-d) = K_{II}^0(1-d)\delta_{II} \tag{27}$$

An example of the cohesive stress σ_{II} *vs* δ_{II} behavior is plotted in Figure 7 (red curve).
In the same way, the apparent frictional stress σ_μ [Eq.(26)] can be expressed, according to Eq.(1), from the effective cohesive stress $\tilde{\sigma}_\mu$ acting on the effective frictional area $\tilde{A}_\mu$ such as:

$$\sigma_\mu = \tilde{\sigma}_\mu \, \frac{\tilde{A}_\mu}{A_0} \tag{28}$$

where the effective frictional stress $\tilde{\sigma}_\mu$ is defined, according to the Coulomb's law, as:

$$0 \leq |\tilde{\sigma}_\mu| \leq \tilde{\sigma}_{\mu_c} = \mu \, \sigma_I \tag{29}$$

where μ is the friction coefficient and $\tilde{\sigma}_{\mu_c} = \mu \, \sigma_I$ corresponds to the shear sliding resistance.
Regarding the effective frictional area $\tilde{A}_\mu$ [Eq.(28)], it is assumed that this area corresponds to a part or all of the damage area $A_d = d \, A_0$ through the function $f(d) = d^p$ with $p \geq 1$, as shown in Fig. 6(b):

$$\tilde{A}_\mu = f(d)A_0 = d^p A_0 \tag{30}$$

Indeed, at the onset of interface damage (*i.e.*, $d \simeq 0$), combination to both compression and shear loading leads to extension (strain) approximately oriented at 45° with respect to the interface plane which, in a case of a quasi-brittle material, generates microcracks oriented perpendicularly to the extension direction. Due to this preferential orientation of microcracks, the shear loading tends to open the microcraks and consequently to cancel the friction effects on the damage area (for $d \simeq 0$, $\tilde{A}_\mu \simeq 0$ and so $\sigma_\mu \simeq 0$). Then, with the increase of interface damage (*i.e.*, $0 < d < 1$), the number of microcracks increases ($0 < A_d < A_0$) and the microcracks progressively coalesce towards a main crack oriented in parallel to the interface plane on which compression and shear loadings act simultaneously. This progressive change in the orientation of cracking (from 45° to 0° with respect to the interface plane) coupled

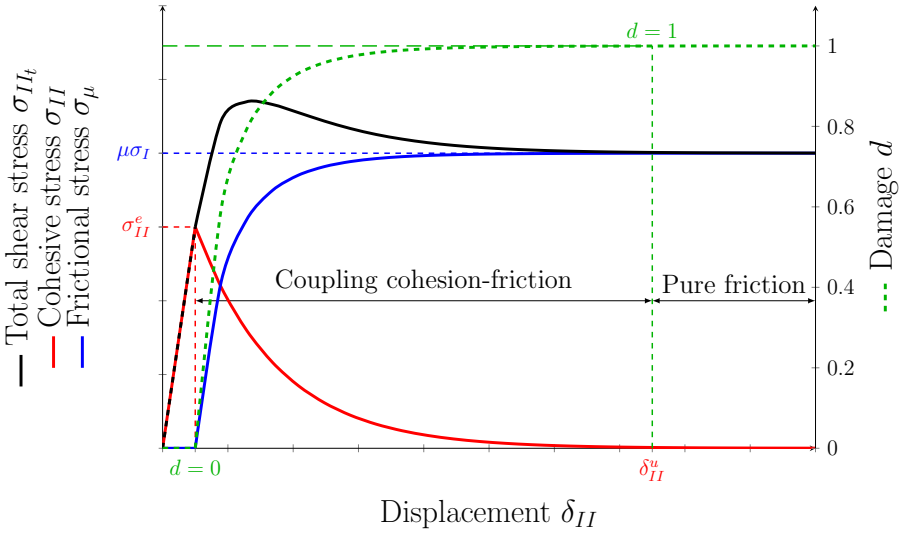

Figure 7: Total shear stress *vs* shear plane displacement response obtained from FCZM and its frictional and cohesive components.

to the increase of damage area lead to an increase of the effective frictional area $\tilde{A}_\mu$ (but $\tilde{A}_\mu \leq A_d$) and hence of the frictional stress σ_μ. Finally, when the failure of interface occurs (*i.e.*, $d = 1$), the effective frictional area $\tilde{A}_\mu$ equals the damage area A_d and both correspond to the whole interface area A_0 which leads to an apparent frictional stress such as: $\sigma_\mu = \mu\, \sigma_I$. Note that the function $f(d) = d^p$ which corresponds to the ratio of the effective frictional area $\tilde{A}_\mu$ over the damage area A_d must correspond to a concave form as shown in Fig. 6(b) since the effective frictional area must not exceed the damage one ($\tilde{A}_\mu \leq A_d$). Nevertheless, another form of concave function could be used to describe $f(d) = \tilde{A}_\mu / A_d$ instead of $f(d) = d^p$ with $p \geq 1$.

Thus, according to Eqs.(29) and (30), the apparent frictional stress σ_μ [Eq.(28)] yields:

$$0 \leq |\sigma_\mu| \leq \sigma_{\mu_c}(d) = f(d)\, \mu\, \sigma_I \tag{31}$$

where $\sigma_{\mu_c}(d)$ corresponds to the *apparent* friction sliding threshold which increases as a function of the damage variable d as shown in Figure 7 (blue curve) and leads to the classical value of the sliding stress $\sigma_{\mu_c} = \mu\, \sigma_I$ when $d = 1$, *i.e.* when the interface is totally failed. Note that, according to Eq.(31), the apparent friction sliding stress $\sigma_{\mu_c}(d)$ can be also expressed as $\sigma_{\mu_c}(d) = \mu(d)\, \sigma_I$ where $\mu(d) = \mu\, f(d) = \mu\, d^p$ can be seen as the apparent

friction coefficient evolving as a function of the damage level.

Finally, according to Eqs.(27) and (28), the apparent shear stress σ_{II_t} [Eq.(26)] yields:

$$\sigma_{II_t} = K_{II}^0(1-d)\delta_{II} + \sigma_\mu \tag{32}$$

where the frictional stress $|\sigma_\mu| \leq \sigma_{\mu_c}(d)$ and where $\sigma_{\mu_c}(d) = d^p\ \mu\ \sigma_I$ corresponds to the apparent sliding resistance. According to Eq.(32), an example of the shear stress σ_{II_t}, resulting from the sum of the cohesive stress σ_{II} and of the shear one σ_μ, is plotted in Figure 7 (black curve). The shape of the obtained σ_{II_t} *vs* δ_{II} response is in agreement that those usually observed experimentally for interfacial failure and describes a smooth transition from a cohesive zone to a pure frictional contact zone.

Moreover, regarding the general shear behavior of the interface given by Eq.(32), when the apparent frictional stress $|\sigma_\mu| < \sigma_{\mu_c}(d)$, the interface displacement is blocked (due to blocking on the effective frictional area $\tilde{A}_\mu$) and hence the cohesive part is no longer loaded (but the cohesive stress σ_{II} remains its value before blocking). Conversely, when $|\sigma_\mu| = \sigma_{\mu_c}(d)$, the interface displacement is possible due to sliding on $\tilde{A}_\mu$ and both cohesive and frictional parts are loaded. This consequences of the rheological model (cohesive spring and a friction pad in parallel as shown Fig. 6(a)) are detailed in the following section from cyclically loading of the interface.

4.2. Response obtained under cyclic loading

In this section, the simulation of a cyclic loading test (obtained from an analytical computation) is carried out to show, from a qualitative point of view, the main features of the proposed constitutive model. The cyclic shear response of the FCZM model is shown in Figure 8. The interface is subjected to a constant compressive normal stress and to tangential cyclic stress through an imposed tangential displacement. Figure 8 shows the evolution of total shear stress $\sigma_{II_t} = \sigma_{II} + \sigma_\mu$ as a function of shear displacement δ_{II} while the evolution of damage variable d is plotted on the secondary axis. The cyclic path is characterized by two loading-unloading cycles (cycle 1: *ABCD* and cycle 2: *EFG)*. In order to ensure an easier description of the loading-unloading behavior, the damage level is kept constant during both cycles.

At the onset of the loading, as long as the cohesive shear stress is lower than the shear strength ($\sigma_{II} < \sigma_{II}^e$), the model remains in the elastic domain (phase *OO'*) and damage variable $d = 0$. When the shear strength σ_{II}^e is

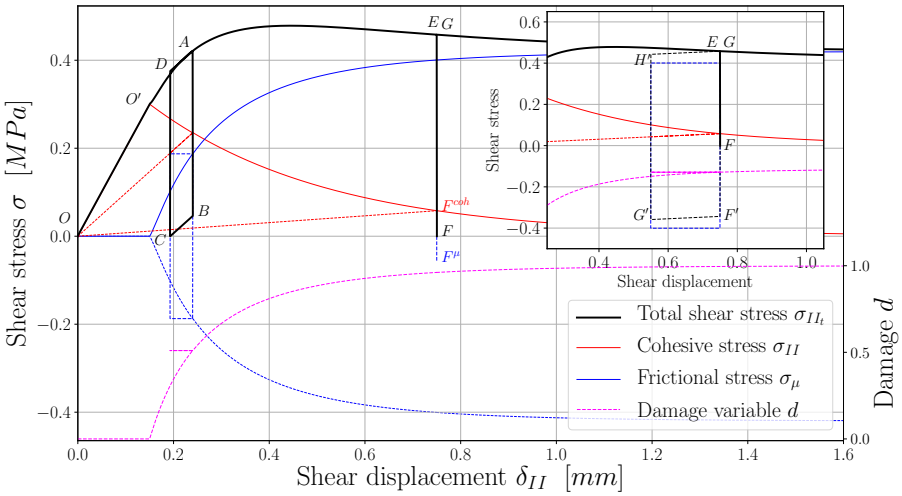

Figure 8: FCZM response expected in the case of two load-unload cycles performed during an unilateral shear test under compression. Inserted graph: example of expected response from a bilateral shear test.

reached (point *O'*), the cohesive stress σ_{II} decreases following the softening exponential law [Eq. (7)] and frictional stress σ_{μ} begins to increase according to the rising of damage variable d, *i.e.*, $\sigma_{\mu} = \sigma_{\mu_c}(d)$. Note that during the phase *O'A* the imposed shear displacement is positive $\dot{\delta}_{II} > 0$ which implies that cohesive stress as well as the frictional one are positive.

Cycle *ABCD-unilateral shear test*: From point A, the displacement δ_{II} is no longer imposed and the interface is unloaded under the sole effect of the cohesive part (this situation corresponds to the realization of an unilateral shear test). This induces a change in the sign of frictional stress ($\sigma_{\mu} < 0$) while the cohesive one remains positive. The fact that $\sigma_{\mu} = -\sigma_{\mu_c}(d)$ leads to a vertical jump of the total shear stress up to point B such as $|\Delta\sigma_{II_t}| = 2\sigma_{\mu_c}(d)$ while the value of the cohesive stress remains constant. From point B, a decrease of the total shear stress is observed up to point C (with $\dot{\delta}_{II} < 0$) which corresponds to a sliding phase of the interface since the value of the cohesive stress is greater than the one of the frictional one $\sigma_{II} > |\sigma_{\mu}|$ where $\sigma_{\mu} = -\sigma_{\mu_c}(d)$ with $d = cte$. The slope of the BC part corresponds to the stiffness of the cohesive spring $K_{II} = K^0_{II}(1-d)$. At point C, the total shear stress value is equal to zero which corresponds to the balance between cohesive and frictional residual stresses such as $\sigma_{II} = -\sigma_{\mu} = -\sigma_{\mu_c}(d)$.
From point C, the displacement δ_{II} is again imposed with $\dot{\delta}_{II} > 0$ and then

the value of frictional stress becomes again positive. Thus, the change in loading direction again induces a jump of the total shear stress up to the point D whose magnitude corresponds to $|\Delta\sigma_{II_t}| = 2\sigma_{\mu_c}(d)$ (since the value of σ_μ changes from $-\sigma_{\mu_c}(d)$ to $\sigma_{\mu_c}(d)$) then an interface sliding occurs from the point D to the point A since the value of the cohesive stress becomes greater to the one of the frictional stress is $\sigma_{II} > \sigma_\mu$ with $\sigma_\mu = \sigma_{\mu_c}(d)$. The slope of the part DA corresponds to the stiffness of the cohesive part $K_{II} = K_{II}^0(1-d)$.
Thus, the cycle $ABCD$ exhibits an hysteresis effect induced by the interface sliding along the part BC and DA and associated dissipated energy from friction effect.

Then, from point A a monotonically loading (i.e., $\dot{\delta_{II}} > 0$ where δ_{II} is imposed) is carried out from point A to point E. The branch AE highlights the rising of damage variable which leads to a softening of the cohesive law and an increase of the frictional stress.

Cycle *EFG-unilateral shear test*: From point E, the displacement δ_{II} is no longer imposed again and, as from point A, the interface is unloaded according to an unilateral shear test in which the displacement can be also induced by the cohesive part of the model. This unloading leads to a change in the sign of frictional stress ($\sigma_\mu < 0$) and induces a *theoretical* vertical jump of the total shear stress such as $|\Delta\sigma_{II_t}| = 2\sigma_{\mu_c}(d)$ while the value of the cohesive stress remains constant and positive.

However, the unloading being carried out under the sole effect of the cohesive spring (unilateral shear test), the fact that the cohesive stress is lesser than the frictional one leads only to a jump of the total shear stress up to $\sigma_{II_t} = 0$ (point F) which corresponds to residual stresses such as $\sigma_\mu = -\sigma_{II}$ with $|\sigma_\mu| < \sigma_{\mu_c}(d)$ meaning the blockage of the interface.
If the interface is then re-loaded from point F ($\dot{\delta_{II}} > 0$ where δ_{II} is imposed), the value of frictional stress becomes again positive and leads to a jump of the total shear stress up to point G induced by the increase of the frictional stress magnitude up to the value $\sigma_{\mu_c}(d)$ (while the cohesive stress value remains constant) from which the interface can slide again but with an increase of the damage variable d.
Thus, from an unilateral shear test, when the cohesive stress becomes lesser than the frictional one, an unloading-loading cycle takes place without hysteresis effect because the sole effect of the cohesive part is not sufficient to induce a sliding of the interface. Conversely, when the cohesive stress is greater than the frictional one, an unloading-loading cycle will exhibit an

hysteresis effect (cycle $ABCD$).

Cycle *EF'G'H'-bilateral shear test* (graph inserted in Fig. 8): Now consider that the unloading is carried out from point E through a bilateral shear test rather than an unilateral one, i.e., the shear displacement is imposed for $\dot{\delta_{II}} < 0$, the total shear stress exhibits effectively the *theoretical* vertical jump of magnitude $|\Delta\sigma_{II_t}| = 2\sigma_{\mu_c}(d)$ up to the point F'. From this point, the interface is then able to slide since the frictional stress is equal $\sigma_\mu = -\sigma_{\mu_c}(d)$ and the interface exhibits a stiffness corresponding to the one of the cohesive part $K_{II} = K_{II}^0(1-d)$ (part $F'G'$). From point G', the interface is re-loaded ($\dot{\delta_{II}} > 0$) and, as previously explained, the reverse of the loading leads to a change in the sign of frictional stress ($\sigma_\mu > 0$) inducing a jump of the total shear stress such as $|\Delta\sigma_{II_t}| = 2\sigma_{\mu_c}(d)$ up to point H' (while the cohesive stress remains constant and positive) from which the interface is again able to slide (since $\sigma_\mu = \sigma_{\mu_c}(d)$) up to point G, exhibiting the stiffness $K_{II} = K_{II}^0(1-d)$. Note that the cycle $EF'G'H'$ exhibits an hysteresis effect linked to the sliding of the interface along the parts $F'G'$ and $H'G$ and the associated dissipated energy.

5. Estimation of cohesive and frictional parameters in the context of masonry : block-mortar interface

Frictional Cohesive Zone Model described in the previous sections is applied in the following in the context of masonry where the knowledge of the mechanical behavior of interface between stone block and joint mortar is particularly relevant with regard to the accurate description of the mechanical behavior of masonry.

FCZM parameters introduced in Sections 3 and 4 are identified on the interface between limestone blocks and hydraulic lime mortar (NHL 3.5)[2]. In the following, the first part presents the main mechanical properties of the masonry constituents: limestone blocks and mortar. Then, a direct tensile test carried out on a duo of limestone blocks assembled by one mortar joint and leading to an estimation of the FCZM Mode I cohesive parameters (K_I^0 $[N/m^3]$, σ_I^e $[N/m^2]$ and G_{f_I} $[J/m^2]$) is presented. Finally, a shear test performed on a triplet of limestone blocks assembled by two mortar joints is described. This test allows estimating the Mode II cohesive parameters

[2]Limestone blocks and hydraulic lime mortar (NHL 3.5) are traditionally used in western region of France for small residential buildings, buildings, churches and bridges

Designation	Quantity	Symbol	Value (CV)	Unit
Limestone	Youngs modulus	E_b	11.1 (15%)	GPa
blocks	Compressive strength	σ_{c_b}	9.5 (26%)	MPa
Hydraulic	Youngs modulus	E_m	*3.95*	GPa
lime	Compressive strength	σ_{c_m}	1.9 (14%)	MPa
mortar	Flexural strength	σ_{f_m}	0.6 (6%)	MPa

Table 1: Mechanical characteristics of limestone blocks and hydraulic lime mortar. The Young's modulus of lime mortar E_m has been estimated by Bisoffi-Sauve (2016) for the same mixture of lime mortar.

(K^0_{II} $[N/m^3]$, σ^e_{II} $[N/m^2]$ and $G_{f_{II}}$ $[J/m^2]$) and frictional parameters (μ [1] and p [1]).

5.1. Characterization of constituents materials

Limestone blocks. The limestone used in this study is typical of the south-west of France and stem from *Pierres de Frontenac* stone quarry. Their compressive properties are determined, according to EN 1926 (2006), from 20 specimens. The blocks tested of nominal dimensions of $100\times100\times100$ mm^3 are positioned between steel plates and 4 extensometers attached directly to the specimen allow to measure strains. Average compressive strength and Youngs modulus obtained from the compression tests are reported in Table 1.

Mortar joints. The lime mortar used in this study is composed of sand, hydraulic lime (NHL 3.5) and water. Proportions by volume of the lime, sand and water in the mixture are estimated by a master stonemason on the basis to 1 part of lime and 3 parts of sand. After that, water is added in the mixture until reaching desired traditional workability. Finally, measured proportions in grams are: 1 (NHL3.5): 6.5 (sand 0-2 [mm]): 1.5 (water). Flexural strength and compressive strength were obtained according to EN 1015-11 (2007) on 8 specimens ($4 \times 4 \times 16$ cm^3). Average flexural strength and compressive strength obtained from lime mortar are reported in Tab. 1.

5.2. Estimation of Mode I cohesive parameters: direct tensile test

5.2.1. Experimental set-up

The cohesive parameters characterizing the Mode I fracture behavior of a block-mortar interface are usually estimated from a direct tensile test (van

Mier, 1996; van der Pluijm, 1999; Almeida et al., 2002; Bisoffi-Sauve, 2016; Sandoval and Arnau, 2017; Bisoffi-Sauve et al., 2019). Despite some differences between the tensile tests proposed in the literature, they can be categorized as a function of their boundaries conditions: rotating supports or fixed supports. Experimental set-up using fixed supports leads to a higher value of the cohesive energy and the tensile strength compared to the one using rotating supports insofar as fixed supports limit flexure effects and induce a more uniform damage of the interface (van Mier, 1996). On this basis, an experimental set-up using fixed supports is chosen in this study to characterize the block-mortar interface in Mode I (Bisoffi-Sauve, 2016; Bisoffi-Sauve et al., 2019).

According to experimental set-up proposed Bisoffi-Sauve et al. (2019), duo of limestone blocks ($10 \times 10 \times 7$ cm^3) assembled by one mortar joint ($10 \times 10 \times 0.7$ cm^3) are directly glued (epoxy resin) inside steel boxes fixed on universal testing machine of 100 kN maximum load capacity thus restricting rotations of blocks during tensile test as shown in Figure 9(b). Experiments are controlled by the opening rate of the mortar joint obtained from the average of displacements measured by four extensometers located on each side of the sample (in the vicinity of corners as proposed by van der Pluijm, 1999) (Figure 9(a)), imposing a opening displacement at constant velocity (0.3 μm/min). In order to limit long term mechanical effects, the opening rate is gradually increased in the post-peak regime to reach 100 μm/min at the end of the test.

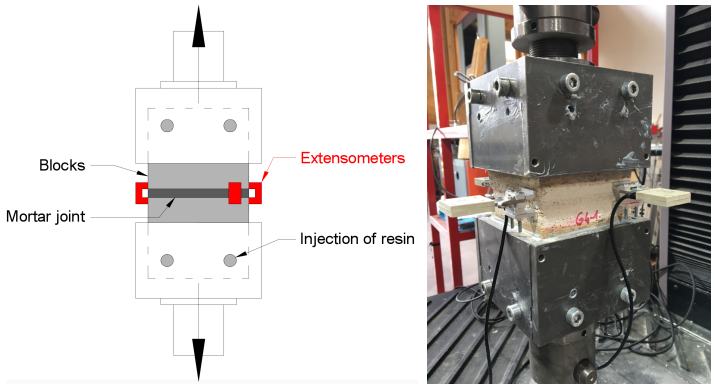

(a) (b)

Figure 9: Tensile test setup: (a) location of extensometers measuring the opening displacement of the mortar joint and (b) picture of test setup

5.2.2. Estimation of Mode I cohesive parameters

As usually observed from direct tensile test, the failure of mortar joint is mainly located at the block-mortar interface. As a consequence, if the tensile stress obtained from the ratio of the tensile load over the specimen nominal cross section is characteristic of the tensile stress applied on the interface, the average displacement measured from the extensometers does not reflect the single opening of the interface. Indeed, as the extensometers are fixed on stone blocks in the immediate vicinity of the joint as shown from Fig. 9(a), the measured displacement value also includes the extension of the mortar joint and, to a lesser extent, the extension of limestone. Thus, knowing the Young's moduli of lime mortar (3.95 GPa, Bisoffi-Sauve, 2016) and limestone (11.1 GPa, Tab. 1), the interface opening is estimated from the average displacement measured from the extensometers in substracting the limestone and joint extensions and this for all values of the tensile stress.
Figure 10(a) exhibits experimental tensile stress *vs* interface opening responses obtained from the tensile test. As previously shown in several studies (van der Pluijm, 1999; Bisoffi-Sauve, 2016; Sandoval and Arnau, 2017; Bisoffi-Sauve et al., 2019), the initial elastic response is followed after the peak stress by a strain negative hardening phase characteristic of the quasi-brittle fracture behavior of the mortar joint and especially the fracture energy required to completely separated the two limestone blocks.

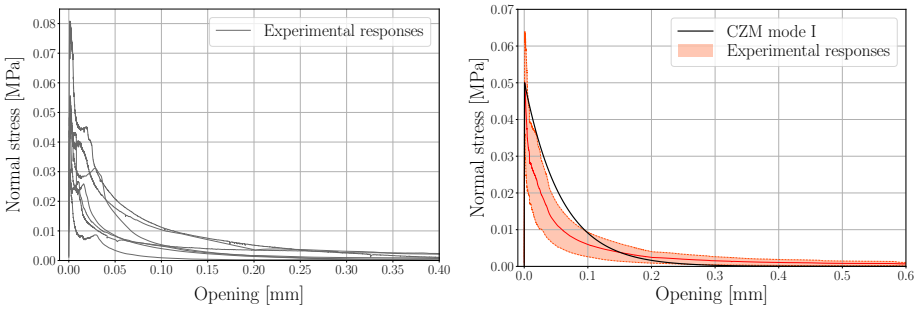

(a) (b)

Figure 10: Direct tensile test results: (a) experimental $\sigma_I - \delta_I$ responses and (b) Mode I cohesive behavior obtained from Eq.(10) compared to the average experimental response more or less one standard deviation

The Mode I cohesive parameters are directly estimated from the tensile stress *vs* opening displacement responses plotted in Fig.10(a). The initial stiffness K_I^0 is estimated from a linear regression of the elastic regime before

Designation	Quantity	Symbol	Value	Unit
Mode I	Initial stiffness	K_I^0	1.21×10^{11}	Pa/m
	Maximum stress	σ_I^e	0.05	MPa
	Cohesive energy	Gf_I	3	J/m^2
Mode II	Initial stiffness	K_{II}^0	2.82×10^{11}	Pa/m
	Maximum stress	σ_{II}^e	0.27	MPa
	Cohesive energy	Gf_{II}	206	J/m^2
Frictional parameters	Frictional coefficient	μ	0.81	1
	Exponent of $f(d)$ function	p	11.0	1

Table 2: FCZM parameters obtained from experimental campaign

the peak stress, the maximum tensile stress σ_I^e is directly obtained from the experimental peak stress while the cohesive energy G_{f_I} is estimated from the area under the $\sigma - \delta$ response. The average of each cohesive parameters is given in Table 2. On this basis and according to Eq.(10), the Mode I cohesive response corresponding to these average parameters is plotted in Figure 10(b) and exhibits a fairly good agreement with the average experimental tensile stress-opening displacement response more or less one standard deviation.

5.3. Mode II characterization: triplet shear test

In literature, there is a large variety of experimental setups allowing combined compression and shear loadings. Among the different proposed setups, one can note (i) the direct shear test used by van der Pluijm (1999) (Fig. 11(a)), (ii) the couplet test (Fig. 11(b)) and (iii) the triplet test requested by EN 1052-3 (2007) shown in Fig. 11(c). The first test (van der Pluijm, 1999) requires very stiff supports to prevent flexure effects while the second one (Lourenço and Ramos, 2004; Abdou et al., 2006) is not symmetrical and can lead to a non homogeneous loading on the mortar joint if the boundary conditions are not perfectly controlled. On this basis, the triplet test appears as the most appropriate insofar as it is symmetric and does not require excessively stiff supports. Furthermore, the simultaneous test of two mortar joints, which may exhibit scattered mechanical properties, leads to the mechanical characterization of a *single* joint whose response corresponds to the average responses of the two joints (Zhang et al., 2008).

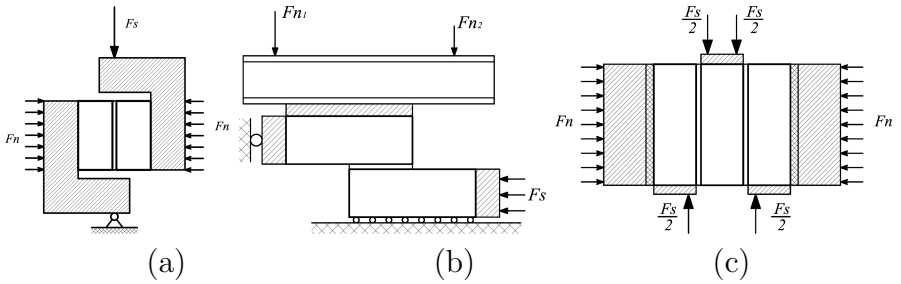

Figure 11: Different types of combined compression and shear test setups: (a) van der Pluijm (1999), (b) couplet test and (c) triplet test (Figure extracted from Lourenço and Ramos, 2004)

5.3.1. Experimental setup

The triplet test is chosen in this study to characterize the frictional and Mode II cohesive properties; this test can exhibits more or less pronounced parasitic loadings. Indeed, a bending loading may appear on the sample especially if the blocks dimension is not sufficient in the direction of the transverse loading (shear loading) as well as a parasitic torsion loading can act on the sample due to the flatness defects of the reference face (supported face) of sample. Improvements of the triplet test (EN 1052-3, 2007) have been recently proposed by Bisoffi-Sauve et al. (2019). The first one, inspired by the EN 13733 (2002) test, is to fix the two end blocks by means of clamping rods in order to prevent bending loading (Fig. 12(b)). The second improvement consists in the modification of one of the supports by the introduction of a degree of freedom in rotation with respect to the axis perpendicular to the joints in order to adapt to flatness defects of the sample supported face.
According to experimental set-up proposed by Bisoffi-Sauve et al. (2019), triplet of limestone blocks ($10 \times 10 \times 10$ cm^3) assembled by two mortar joints ($10 \times 10 \times 0.7$ cm^3) are initially submitted to a compression loading leading to a normal stress on the mortar joint and then fixed on universal testing machine of 100 kN maximum load capacity at the end blocks. Three normal stress levels are applied on the mortar joint: 0.4 MPa, 0.6 MPa and 0.8 MPa. Specimens are tested by imposing a vertical displacement to the central block leading to shearing of the mortar joints. Experiments are controlled by the shear plane displacement rate of the mortar joints obtained from the average of displacements measured by four extensometers located on both sides of the sample in the immediate vicinity of the joints (Fig. 12(a)). At the onset of the test, the velocity of the average shear plane displacement is imposed

to 0.5 μm/min then is gradually increased in the post peak regime to reach 100 μm/min at the end of the test.

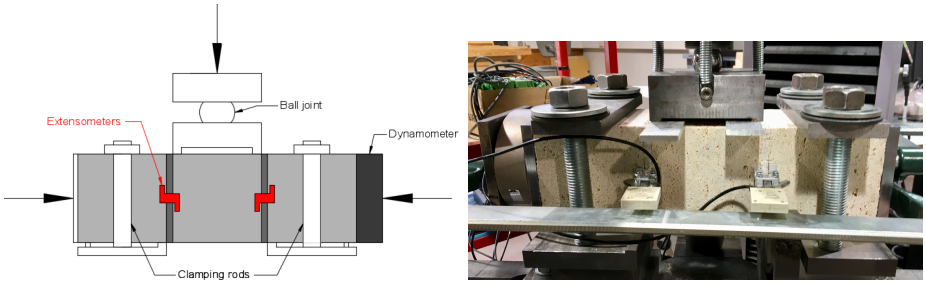

(a) (b)

Figure 12: Combined compression and shear test setup: (a) position of extensometers and (b) picture of the triplet test

5.3.2. Estimation of frictional and Mode II cohesive parameters

As previously observed from tensile test, shear test exhibits also failures mainly located of the block-mortar interface. Thus, the shear plane displacement corresponding to the interface needs to be estimated from the average displacement measured from the four extensometers by substracting the contributions of the mortar joint and of the limestone knowing the shear moduli of materials ($G = E/[2(1+\nu)]$ with a Poisson's ratio of 0.2). Moreover, the shear stress is obtained by dividing the vertical load applied on the central block by the nominal cross section of both joints while the normal stress is estimated from the compression load divided by the nominal cross section of one joint. As the effective section of the joints gradually decreases according to the shear plane displacement, the values of the shear and normal stresses are updated as a function the shear displacement value.

Six to seven specimens have been tested for each normal stress level (0.4, 0.6 and 0.8 MPa). From the experimental shear stresses *vs* shear displacement responses of the block-mortar interface (i.e., σ_{II_t} *vs* δ_{II}) obtained for each normal stress level, the average shear stress and the standard deviation of this one $\Delta\sigma_{II_t}$ are computed as a function of the shear plane displacement δ_{II} and are plotted in Figure 13(a): blue color for experimental ($\sigma_{II_t} \pm \Delta\sigma_{II_t}$) *vs* δ_{II} response obtained for $\sigma_N = 0.4$ MPa, green color for $\sigma_N = 0.6$ MPa and red color for $\sigma_N = 0.8$ MPa.

First of the mechanical parameters estimated from the experimental re-

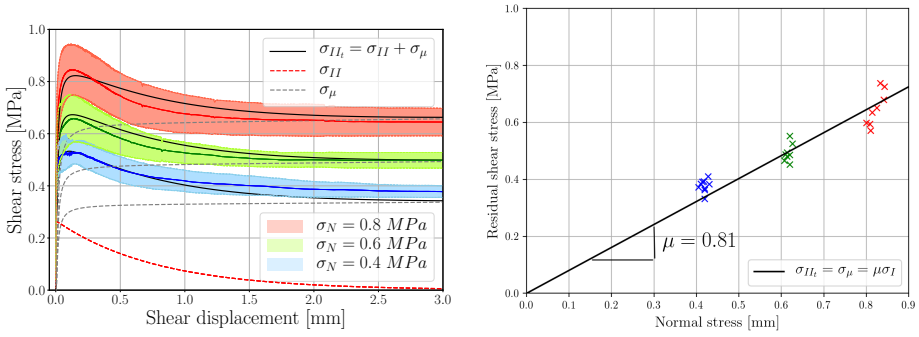

(a) (b)

Figure 13: Experimental results obtained from improved triplet shear tests: (a) average experimental shear stress *vs* shear displacement responses of the block-mortar interface and (b) estimation of friction coefficient linear regression

sponses plotted in Fig. 13(a), the friction coefficient μ is obtained from a linear regression of the residual stress (*i.e.*, the constant stress observed for large shear plane displacements and for which there is no longer cohesion of the interface) as a function of the normal stress with a y-intercept forced to zero as shown in Figure 13(b). Indeed, when there is no longer cohesion of the block-mortar interface (i.e., $d = 1$ for the whole interface area), the residual stress is expected to be equal to the effective frictional stress such as $\sigma_{II} = \sigma_\mu = \tilde{\sigma}_{\mu_c} = \mu\sigma_I$. As shown from Fig. 13(b), the friction coefficient of the interface limestone block-lime mortar is estimated to $\mu = 0.81$ and reported in Table 2.

The second parameter which can be directly estimated from the experimental responses plotted in Fig. 13(a) is the initial stiffness K_{II}^0 of the block-mortar interface. The initial stiffness K_{II}^0 is estimated from linear regression of the initial elastic part of the experimental responses and the value obtained is reported in Table 2.

Contrarily to initial stiffness K_{II}^0 and friction coefficient μ, the shear strength σ_{II}^e, the total cohesive energy $G_{f_{II}}$ and the exponent p of the power function $f(d)$ cannot be directly identified from the experimental responses. Latter cohesive and frictional parameters are estimated by matching the experimental responses according to the theoretical behavior expected from FCZM described in Eq.(32). Nevertheless, in the mechanical response of the block-mortar interface, the accurate description of the stress and displacement at

peak load appear relevant while the accuracy of the description of the response as a whole appears less important. Thus, a large quantity of σ^e_{II}, $G_{f_{II}}$ and p combinations are tested and, for each combination, a first normalized square deviation between experimental and numerical peak loads (stress and displacement) are computed and a second one is computed from the whole experimental and numerical responses. On this basis, in order to ensure a description of the peak load with accuracy, a weight of 5/10 is given arbitrarly to the normalized square deviation linked to peak load value and 4/10 is given (arbitrarly) to the one linked to the displacement at peak load (*i.e.* a weight of 9/10 for peak load) while a weight of 1/10 is considered for the normalized square deviation corresponding to the whole response. The fit-

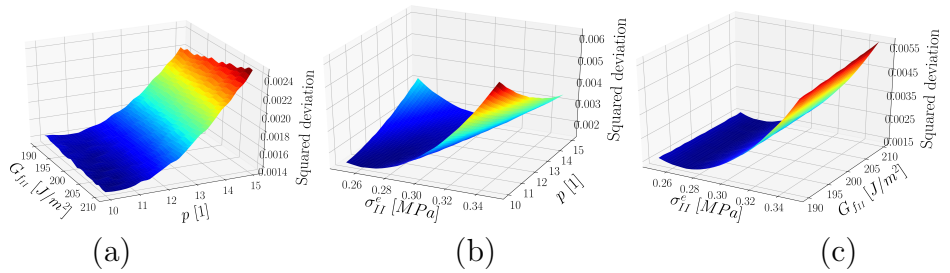

Figure 14: Square deviation evolution for: (a) $\sigma^e_{II} = 0.27$ MPa, (b) $G_{f_{II}} = 206$ J/m^2 and (c) $p = 11$

ting method proposed here leads to a single combination solution as shown in Figure 14 even if Mode II cohesive energy $G_{f_{II}}$ has a lesser impact on the best response compared to shear strength σ^e_{II} and exponent p of the power function $f(d)$. Cohesive parameters and frictional one are reported in Table 2 while the shear stress *vs* shear plane displacement of the block-mortar interface obtained from FCZM [Eq. 32] are plotted as black color curves in Fig. 13(a).

Finally, let us emphasize that the experimental shear stress *vs* shear plane displacement responses of the block-mortar interface are described from FCZM [Eq. 32] with a reasonable accuracy and especially from a single set of cohesive parameters (*i.e.* independent of the normal stress applied on the interface).

Moreover, note that the FCZM model presented here will be able to describe the flattening of the shear stress *vs* shear displacement response usually observed in the case of high normal stress level as shown from Fig.13(a) (or from Fig.10b in D'Altri et al, 2019). Indeed, as it can be deduced from Fig.

13(a), for large critical frictional stress $\sigma_{\mu_c} = \mu\sigma_I$ compared to the interfacial shear strength σ_{II}^e, it is expected that the peaked shape of the response vanishes to the benefit of a response close to the one associated with the frictional stress. In the opposite case, *i.e.* when the normal stress to the interface is weak (Fig.10b in D'Altri et al, 2019), the FCZM proposed here will be able to exhibit the peaked shape of the response because the cohesive stress becomes predominant compared to the frictional one.[3]
Note that the flattening of the shear stress *vs* shear displacement response with respect to the normal stress value (exhibited by the FCZM proposed here) is not reachable by *classical* FCZM (*i.e.* based on the superimposition of the full friction stress and the cohesive one) because, whatever the normal stress is, the difference between the peak stress and the critical frictional stress remains constant and equal to the cohesive shear strength.

The two characterization tests proposed here (direct tensile test on duo and shear test on triplet) are designed to lead to almost uniform loading along the block-mortar interface. In both tests, the damage tends to spread uniformly over the entire surface of the interface and hence allows to estimate the behavior of the assembly block-joint-block and especially the one of the interface block mortar at the mesoscopic scale. If from a theoretical point of view, FCZM can be used at the microscopic scale (local response of the material), the estimate of cohesive and frictional parameters of FCZM obtained from both tests and given in Table 2 is performed at the mesoscopic scale, with the aim of using it on this scale. Note that, the notion of mesoscopic scale is important for the future use of FCZM for masonry simulations and especially in a code based on Discrete Element Method (DEM). Indeed, in the case of large structure sizes simulations, only a few contact points are usually considered on each face of the blocks and hence each contact point is associated with a surface of the block-mortar interface of several tens of square centimeters.

[3]The flattening phenomenon experimentally observed on the shear stress *vs* shear displacement response with respect to the normal stress level is at the source of the underestimation of the cohesive behavior (and especially of the cohesive energy) when this one is simply estimated by subtracting the full friction stress from the total shear stress *vs* shear displacement response because the part supposed to correspond to the cohesive behavior decreases with respect to normal stress level.

In the following section, the ability of FCZM to describe an experimental cyclic shear loading applied on the triplet specimen is shown and discussed.

6. Triplet shear test under unilateral cyclic loading: experimental *vs* numerical responses

In order to use the FCZM in the case of complex loading, the model was implemented in the LMGC90 code (Dubois et al., 2011) based on the Discrete Element Method (DEM) and more specifically on the *Non Smooth Contact Dynamics* (Moreau, 1988; Jean, 1999). As a first attempt, FCZM is used to describe the experimental response obtained from unilateral cyclic shear loading applied on triplet specimen.

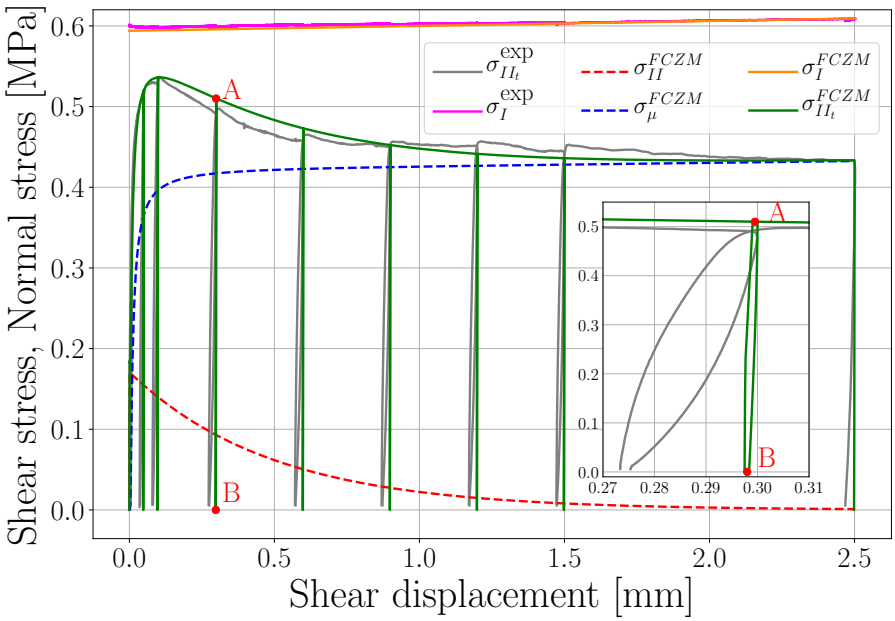

Figure 15: Experimental and simulated shear stress *vs* shear plane displacement response of the joint and block-mortar interface obtained from an unilateral cyclic loading.

Using the same experimental setup as the one described in Section 5.3, a cyclic loading test leads to the typical shear stress *vs* shear plane displacement response plotted in Figure 15. Note that the shear plane displacement corresponds here to the one of the mortar joint and of the block-mortar interface, *i.e.* only the contribution of the limestone is subtracted from the

Designation	Quantity	Symbol	Value	Unit
Mode II	Initial stiffness	K_{II}^0	3.4×10^{11}	Pa/m
	Maximum stress	σ_{II}^e	0.17	MPa
	Cohesive energy	Gf_{II}	83	J/m^2
Frictional parameters	Frictional coefficient	μ	0.71	1
	$f(d)$ function exponent	p	15	1
	Normal stress	σ_I	0.59	MPa

Table 3: FCZM parameters fitted to describe the typical response obtained from the unilateral cyclic shear loading applied on triplet specimen (Fig. 15)

average displacement measured from the four extensometers. The experimental response plotted in Fig.15 is obtained for a normal stress value of 0.6 MPa and exhibits jumps of the shear stress associated with each onset of loading and unloading phases as theoretically expected from the discussion proposed in Section 4.2.

A 2D simulation of the unilateral shear test is carried out using LMGC90 software considering rigid blocks and two mortar joints modelled by deformable elements meshed with 25 regular quadrangles in the height and 2 in the width as shown in Fig. 16. Young's modulus of joint elements is $E_j = 3.95$ GPa while Poisson's ratio $\nu = 0.2$. Moreover, the experimental joint failure being mainly interfacial, only the interfaces block-joint associated with the central block are considered, the other two interfaces are coupled at rigid blocks to prevent the relative displacement between ends block and joints. Note that the blocks being modelled from rigid bodies, their geometry is not relevant in this simulation, only the geometry and dimensions of the joints need to correspond to experimental ones. Two contact points per finite element are considered leading to a total of 50 contact points along each interface. The modelling of the unilateral cyclic shear test from LMGC90 code is performed by first applying the normal force to the end blocks and then by loading the central block through the contact of a rigid body (not shown in Fig. 15) on which a vertical velocity-time function reproducing experimental loading cycles is imposed. The shear loading procedure by contact allows to lose contact with the central block and thus to achieve a complete shear unloading of the specimen between two consecutive cycles.

Firstly, FCZM parameters are fitted, according to the procedure described in Section 5.3.2, to describe the envelope of the typical experimental shear stress *vs* shear plane displacement response. The simulated σ_{II_t} *vs* δ_{II} re-

sponse is plotted in Figure 15 and its envelope appears to be consistent with the experimental one. Note that FCZM parameters obtained to describe the experimental response are given in Table 3 and differ from those given in Table 2 because they correspond to a given experimental triplet specimen while those given in Tab. 2 result from the fitting procedure applied on a set of triplets (Section 5.3.2).
In a second time, the cyclic loading is simulated and the obtained response is plotted in Fig. 15. As shown from Fig. 15, the onset of experimental loading and unloading phases and associated residual displacements are described by the model with a reasonable accuracy. Let us remember that a

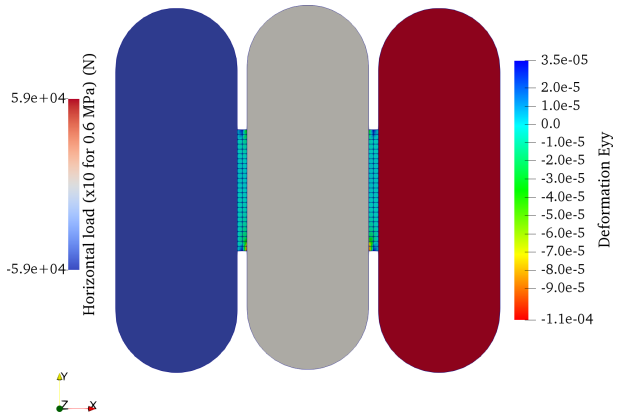

Figure 16: Numerical model of the triplet shear test (LMGC90)

jump of the total shear stress σ_{II_t} associated with a blockage of the interface displacement is expected at the onset of loading and unloading phases when the cohesive stress σ_{II} becomes lesser than the critical frictional one $\sigma_{\mu_c}(d)$ which is the case here for all the loading and unloading phases as shown from the evolutions of cohesive stress and of the critical frictional one plotted in red color and blue color respectively in Fig. 15. Moreover, as shown from the inserted graph in Fig. 15 which corresponds to a zoom of the onset of loading and unloading phases A-B, the experimental and numerical responses are characterized by a slope which correspond to the stiffness of the joint (the interface displacements being mainly blocked during loading-unloading phases). The fact that the experimental stiffness of the joint differs from the numerical one (inserted graph in Fig.15) could be explained by the fact that, experimentally, the damage is not fully located on the interfaces but also diffuses in the mortar joint inducing a decrease of the joint stiffness which is

not taken into account in the simulation. Moreover, experimental cycles exhibit more pronounced hysteresis loops than simulated ones which seems to indicate the existence of dissipative mechanisms other than the only damage and friction at the block-mortar interface. Finally, note that thin hysteresis loops exhibited by the simulation are only due to the fact the contact points along the interfaces do not show the same $(\sigma_{II_t}, \delta_{II})$ state at the same time in the sense that, if the the majority of the contact points are blocking, some of contact points are still sliding.

7. Conclusions

In this paper, a general Frictional Cohesive Zone Model dedicated to quasi-brittle failure is proposed. The model is based on pure Mode I and Mode II cohesive behaviors whose softening part is described from an exponential function and on Coulomb's law for the frictional behavior.

Under combined traction and shear loadings, the coupling between Mode I and Mode II cohesive behaviors is obtained from two criteria (damage initiation criterion and failure criterion) proposed by Camanho et al. (2003). The analytical study of the cohesive energy dissipated as function of loading path emphasizes that proposed FCZM exhibits a load path dependency which is in agreement with the one observed in quasi-brittle fracture.

Under combined compression and shear loadings, taking inspiration of several preceding works which revised the assumption of simple superposition of full friction and Mode II cohesive behavior, a coupling between friction effect and cohesive behavior is proposed through the damage variable (single internal variable of the FCZM). Indeed, the damage variable gives an estimation of the effective damage area of the interface and we assume here that the effective friction phenomenon takes place on part of all of the damage area as a function of the damage level. On this basis, FCZM exhibits a progressive rising friction stress as a function of the shear plane displacement which leads to a smooth transition from a cohesive zone to a pure contact zone.

Applied to the context of masonry, FCZM can be fully characterized from two fracture tests carried out on small masonry assemblages. Mode I cohesive parameters are estimated from a tensile fracture test carried out on duo of limestone blocks assembled by one lime mortar joint while the Mode II cohesive parameters and the frictional ones are estimated from a shear test performed on a triplet of limestone blocks assembled by two lime mortar

joints. If the estimation of Mode I cohesive parameters is directly obtained from the tensile stress *vs* interface opening response, the estimation of Mode II and frictional parameters needs, firstly, the estimate of the friction coefficient from the residual shear stresses with regard to the normal stress imposed on the joint, then, an indirect estimation procedure needs to be used in order to simultaneously determine the Mode II cohesive parameters and the parameter driving the evolution of the friction stress as a function of the damage variable value. The proposed methodology is discussed and it is shown that this one leads to a single set of cohesive and frictional parameters to describe the shear stress *vs* shear plane displacement responses. Moreover, FCZM describes the flattening of the shear stress *vs* shear displacement response as a function of the normal stress value usually observed experimentally. Such a phenomenon is not possible to describe from *classical* FCZM (*i.e.* based on the superimposition of the full friction stress and the cohesive one) because, whatever the normal stress is, the difference between the peak stress and the critical frictional stress remains constant and equal to the cohesive shear strength in these models.

Finally, the FCZM is implemented in LMGC90 discrete element code and is used to simulate the experimental response of an unilateral cyclic shear test carried on a triplet of lime stone assembled by two lime mortar joints. The envelope of a typical shear stress *vs* shear plane displacement response is described by the FCZM with a reasonable accuracy as well as the experimental stress jumps and corresponding residual displacements associated with the onset of the loading and unloading phases.

FCZM will be used shortly to simulate the mechanical behavior of masonry panels submitted to constant vertical load (three vertical load levels) and to a progressive horizontal load up to failure of the panel. Indeed, this kind of loading applied on masonry panels lead to various loading modes as a function of the considered area of the panel (traction, compression, shear, combined traction or compression and shear) and hence simulations of such experiments should constitute a large base of validation of the model.

8. Acknowledgments

The authors thank AIA Ingénierie company (Architectes Ingénieurs Associés) and escially Alain Popinet (Agency Director) and the French National Association of Research and Technology (ANRT) for supporting the study (2016/1369). We also thank Bernard Solbes for his technical expertise in

experimental tests. The experimental part of the study has been performed from the Xyloplate platform equipments - Equipex XYLOFOREST (ANR-10-EQPX-16) - supported by the French National Research Agency (ANR).

References

Abdou, L., Ami Saada, R., Meftah, F., Mebarki. A., 2002. Experimental investigations of the joint-mortar behavior. Mechanics Research Communications 33, 370-384.

Acary, V., Monerie, Y., 2006. Nonsmooth fracture dynamics using a cohesive zone approach. Rapport de Recherche INRIA 6032.

Almeida, J.C., Lourenço, P.B., Baros, J.A., 2002. Characterization of brick and brickmortar interface under uniaxial tension. International Seminar on Structural Masonry for Developing Countries VII, 67–76.

Alfano, G., Sacco, E., 2006. Combining interface damage and friction in a cohesive-zone model, International Journal for Numerical Methods in Engineering 68,542-582.

Baek, H., Park, K., 2018. Cohesive frictional-contact model for dynamic fracture simulations under compression. International Journal of Solids and Structures 144-145, 86–99.

Bisoffi-Sauve, M., Morel, S., Dubois, F., 2019. Modelling mixed mode fracture of mortar joints in masonry buildings. Engineering Structures 182, 316–330.

Bisoffi-Sauve, M., 2016. Etude des ouvrages maonnés en pierre par la méthode des éléments discrets : caractérisation et modélisation du comportement cohésif des joints. PhD Thesis, Université de Bordeaux.

van den Bosch, M.J., Schreurs, P.J.G., Geers, M.G.D., 2006. An improved description of the exponential Xu and Needleman cohesive zone law for mixed-mode decohesion. Engineering Fracture Mechanics 73, 1220–1234.

Camacho, G.T., Ortiz, M., 1996. Computational modelling of impact damage in brittle materials. International Journal of solids and structures 33, 2899–2938.

Camanho, P.P., Davila, C.G., de Moura, M.F., 2003. Numerical simulation of mixed-mode progressive delamination in composite materials. Journal of Composite Materials 37, 14151438.

Chaboche, J.-L., Girard, R., Schaff, A., 1997. Numerical analysis of composite systems by using interphase/interface models. Computational Mechanics 20, 3–11.

D'Altri, A.M., de Miranda, S., Castellazzi, G., Sarhosis V., 2018. A 3D detailed micro-model for the in-plane and out-of-plane numerical analysis of masonry panels. Computers and Structures 206, 18–30.

D'Altri, A.M., Messali, F., Rots, J., Castellazzi, G., de Miranda, S., 2019. A damaging block-based model for the analysis of the cyclic behaviour of full-scale masonry structures. Engineering Fracture Mechanics 209, 423–448.

Dimitri, R., Trullo, M., De Lorenzis, L., Zavarise, G., 2015. Coupled cohesive zone models for mixed-mode fracture: A comparative study. Engineering Fracture Mechanics 148, 145–179.

Dubois, F., Jean, M., Renouf, M., Mozul, R., Martin, A., Bagnéris, M., 2011. LMGC90. 11ème Colloque National en Calcul des Structures, Giens, France.

EN 1015-11, 2007. Methods of test for mortar for masonry - Part 11: Determination of flexural and compressive strength of hardened mortar. AFNOR.

EN 1052-3, 2007. Methods of test for masonry - Part 3: Determination of initial shear strength. AFNOR.

EN 1926, 2006. Natural stone test methods - Determination of uniaxial compressive strength. AFNOR.

EN 13733, 2002. Products and systems for the protection and repair of concrete structures - Test methods - Determination of the durability of structural bonding agent . AFNOR.

Freddi, F., Sacco, E., Serpieri, R., 2017. An enriched damage-frictional cohesive-zone model incorporating stress multi-axiality. Meccanica, 1–20.

Hillerborg, A., Modéer, M., Petersson, P.-E., 1976. Analysis of crack formation and crack growth in concrete by means of fracture mechanics and finite elements. Cement and concrete research 6, 773–781.

Högberg, J. L., 2006. Mixed mode cohesive law. International Journal of Fracture 141, 549–559.

Jean, M., 1999. The non-smooth contact dynamics method. Computer Methods in Applied Mechanics and Engineering 177, 235–257.

Lourenço, P.B., Ramos, L.F., 2004. Characterization of cyclic behavior of dry masonry joints. Journal of Structural Engineering 130, 779–786.

van Mier, J.G.M., 1996. Fracture Processes of Concrete. CRC Press.

Moreau, J.J., 1988. Unilateral contact and dry friction in finite freedom dynamics. Nonsmooth mechanics and Applications, Vienna: Springer, 1–82.

Morel, S., Lespine, C., Coureau, J.-L., Planas, J., Dourado, N., 2010. Bilinear softening parameters and equivalent LEFM R-curve in quasibrittle failure. International Journal of Solids and Structures 47, 837–850.

van der Pluijm, R., 1993. Shear behavior of bed joints. Proceedings of 6th North American masonry conference, 125–136.

van der Pluijm, R., 1999. Out-of-plane bending of masonry: behavior and strength. PhD Thesis, Technische Universiteit Eindhoven.

Raous, M., Monerie, Y., 2002. Unilateral contact, friction and adhesion: 3D cracks in composite materials, 3rd Contact Mechanics. International Symposium, Contact Mechanics, J.A.C. Martins and M.D.P. Marques (Eds), 333–346.

Sandoval, C., Arnau, O., 2017. Experimental characterization and detailed micro-modeling of multi-perforated clay brick masonry structural response. Materials and Structures 50, 34.

Snozzi, L., Molinari, J-F., 2013. A cohesive element model for mixed mode loading with frictional contact capability. International Journal for Numerical Methods in Engineering 93, 510–526.

Spring, D.W., Paulino, G.H., 2015. Computational homogenization of the debonding of particle reinforced composites: The role of interphases in interfaces. Computational Materials Science 109, 209–224.

Xu, X.-P., Needleman, A., 1993. Void nucleation by inclusion debonding in a crystal matrix. Modelling and Simulation in Materials Science and Engineering 1, 111-132.

Yuen, T.Y.P., Deb, T., Zhang, H., Liu, Y., 2019. A fracture energy based damage-plasticity interfacial constitutive law for discrete finite element modelling of masonry structures. Computers and Structures 220, 92–113.

Zhang, S., Taheri Mousavi, S.M., Richart, N., Molinari, J.-F., Beyer, K., 2017. Micro-mechanical finite element modeling of diagonal compression test for historical stone masonry structure. International Journal of Solids and Structures 112, 122–132.

Zhang, J., Liang, N.-G., Deng, S.-C., Liu, J.-X., Liu, X.-Y., Fu, Q., 2008. Study of the Damage-induced Anisotropy of Quasi-brittle Materials using the Component Assembling Model. International Journal of Damage Mechanics 17, 197–221.

Zimmermann, T., Strauss, A., Bergmeister, K., 2005. Structural behavior of low- and normal-strength interface mortar of masonry. Materials and Structures 45, 829–839.

Zucchini, A., Lourenço, P.B., 2002. A micro-mechanical model for the homogenisation of masonry. International Journal of Solids and Structures 39, 3233–3255.

Frictional Cohesive Zone Model for quasi-brittle fracture: Mixed-mode and coupling between cohesive and frictional behaviors

V. Venzal[a,c], S. Morel[a,*], T. Parent[a], F. Dubois[b]

[a] *Université de Bordeaux, UMR5295, Institut de Mécanique et d'Ingénierie-Bordeaux (I2M), Dépt. Génie Civil et Environnemental (GCE), Bordeaux F-33000, France*
[b] *LMGC, Univ Montpellier, CNRS, Montpellier, France*
[c] *AIA Ingénierie, 10 rue Ariane, Bât C, 33700 Mérignac, France*

Abstract

In this study, a general frictional cohesive zone model (FCZM) dedicated to quasi-brittle fracture is proposed to describe the mechanical response of an interface under combined traction or compression and shear loadings. Under combined traction and shear loadings, mixed-mode $I + II$ cohesive zone model, as proposed by Camanho et al. (2003), is used to express the mixed-mode response of the interface and the dependence to the loading path consistent to the one expected in quasi-brittle fracture. Under combined compression and shear loadings, the novelty lies in the proposed coupling between Mode II cohesive behavior and frictional behavior based on the damage level leading to a progressive rising of the frictional stress associated with the softening part of the cohesive behavior of the interface. FCZM thus describes a smooth transition from a cohesive zone to a pure frictional contact zone. Applied to the masonry context, this general FCZM can be fully characterized through two fracture tests carried out on small masonry assemblages. Finally, FCZM is implemented in LMGC90 discrete element code and used to simulate the experimental response of an unilateral cyclic shear test carried out on a triplet of limestone blocks assembled by two mortar joints.

Keywords: Quasi-brittle fracture, Cohesive zone model, Mixed-mode, Frictional behavior, Discrete Element Method, Masonry assemblages

*stephane.morel@u-bordeaux.fr

1. Introduction

The basic hypothesis of cohesive zone models is that failure can be described through a fictitious surface crack (which is usually characterized by a zero thickness interface) which transmits normal and shear stresses. The magnitudes of normal and shear stresses are described from functions (monotonically decreasing) of the opening displacement (Mode I) and of the shear plane displacement (Mode II) of the interface.

In literature there is a large variety of Cohesive Zone Models (CZM) which can be differentiated according to the shape of their softening parts: rigid-linear (Camacho and Ortiz, 1996; Snozzi and Molinari, 2013), bi-linear (Hilleborg et al., 1976; Camanho et al., 2003; Högberg, 2006), tri-linear (Morel et al., 2010; Bisoffi-Sauve et al., 2019) and exponential CZM (Xu and Needleman, 1993; van den Bosch et al., 2006). In those models, the cohesive stresses decrease (after an elastic domain) according to the rising of a damage variable (scalar) usually noted as d. Mode I and Mode II cohesive behaviors are generally described according to softening functions exhibiting a similar shape.

In the case of combined traction and shear loadings, Mode I and Mode II cohesive behaviors can be coupled or uncoupled. Uncoupled CZM are typically used when interface separation occurs in a single predefined direction, while coupled CZM are used for complex loading leading simultaneously to opening and shear plane displacements of the interface. Coupled CZM generally differ according to the criteria used to describe the mixed-mode $I+II$ failure and the dependence (or not) to the loading path exhibited by the material fracture (van den Bosch et al., 2006; Camanho et al., 2003; Dimitri et al., 2015).

In the case of combined compression and shear loadings, the contribution of the friction phenomenon complicates the analysis of the respective contributions of the frictional and cohesive behaviors in the mechanical response of the interface. As such, if the cohesive behavior is estimated by simply subtracting the value of the *full* friction stress from the total shear stress-shear plane displacement response (Freddi et al., 2017; Baek and Park, 2018; Bisoffi-Sauve et al., 2019; Yuen et al., 2019), the resulting Mode II cohesive energy is usually underestimated and associated with a physically inconsistent dependence to the normal stress. Note that such an assumption of

superimposition of *full* friction stress and cohesive stress leads to consider that the cohesive behavior is only activated if the full friction threshold is reached or, in other words, that the friction effect takes place while the cohesive capacity of interface is still intact, which appears to be physically inconsistent. To overcome this issue, several authors (Chaboche et al., 1997; Snozzi and Molinari, 2013; Spring and Paulino, 2015; D'Altri et al, 2018) have proposed phenomenological evolutions of the friction stress as a function of the shear plane displacement superimposed to the cohesive behavior. Nevertheless, even if these *frictional* cohesive zone models allow a better description of experimental stress-displacement responses, assuming a friction stress function of the shear plane displacement is not physically based since frictional effect is expected to depend only on the normal stress, the friction coefficient and the area of the surface on which it acts. A coupling based on the damage part of the interface on which the frictional phenomenon can physically act appears more relevant (Raous and Monerie, 2002; Acary and Monerie, 2006; Alfano and Sacco, 2006).

On this basis, we propose a general Frictional Cohesive Zone Model dedicated to quasi-brittle fracture describing the mechanical response of an interface under combined traction or compression and shear loadings. In Section 2, the cohesive laws with exponential softening used for pure Mode I and Mode II fractures are presented and a reminder of the physical meaning of the damage variable driving the softening part is proposed. On this basis, under combined traction and shear loadings (Section 3), mixed-mode $I + II$ cohesive zone model proposed by Camanho et al. (2003) is used to express the mixed-mode response of the interface and the dependence to the loading path consistent to the one expected in quasi-brittle fracture. Under combined compression and shear loadings (Section 4), the novelty lies in the proposed coupling between cohesive and frictional behaviors which is obtained through an estimate of the effective frictional area, itself estimated from the damage variable. A first illustration of the response obtained from FCZM under cyclic shear loading is proposed. In Section 5, the FCZM is used in the context of masonry and two characterization tests allowing the estimation of all the cohesive and frictional parameters of a block-mortar interface are described. The methodology used to estimate simultaneously the frictional and Mode II cohesive parameters is particularly discussed. Finally, in Section 6, the FCZM is implemented in LMGC90 discrete element code and used to simulate the experimental response of an unilateral cyclic shear test carried out on a triplet of limestone blocks assembled by two mortar joints.

2. Cohesive law with exponential softening

The accurate simulation of interfacial failure in quasi-brittle materials needs to use an appropriate cohesive law allowing in particular the description of (i) the negative hardening expected for the tension and shear stress-displacement responses of the interface, (ii) the dependence on the loading path and of (iii) the strong dissymmetry of tensile and shear fracture properties.

Among the different functions used to describe the softening behavior in CZM, exponential softening allows fitting, with a reasonable accuracy, of the negative and concave hardening function expected in quasi-brittle fracture as shown in Figure 1. In this study, one proposes to describe the Mode I and Mode II cohesive behaviors from the same shape of cohesive law (exponential softening) as shown in Figure 1 where $i = \{I, II\}$. The initial elastic behavior is characterized by the stiffness K_i^0 [N/m^3] and the tensile ($i = I$) or shear ($i = II$) strength σ_i^e [N/m^2]. The stress σ_i as well as the stiffness K_i decrease continuously reflecting the softening behavior of the interface (Fig. 1). The decrease of the stiffness K_i from its initial value K_i^0 (and

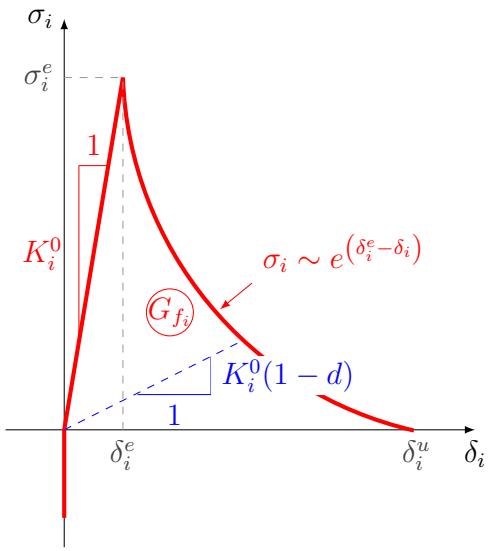

Figure 1: Cohesive law with exponential softening

consequently, the one of the cohesive stress σ_i from the strength σ_i^e) is driven by a damage variable d (scalar variable). The damage variable d reflects the

level of the mechanical degradation of the interface which can be described through the development of crack surface. In this way and particularly in Mode I, d is defined as the ratio of the cracked surface A_d [m^2] over the whole interfacial surface area A_0 [m^2], *i.e.,* $d = A_d/A_0$. Thus $0 \leq d \leq 1$, $d = 0$ corresponding to an intact interface ($A_d = 0$) while $d = 1$ reflects the overall failure of the interface ($A_d = A_0$). Thus, for a given damage level d, the load F_i transmitted by the interface can be expressed either with the *apparent* stress σ_i applied on the whole interface surface A_0 or with the *effective* stress $\tilde{\sigma}_i$ applied on the healthy surface of the interface $\tilde{A}$:

$$F_i = \tilde{\sigma}_i \tilde{A} = \sigma_i A_0, \tag{1}$$

where the healthy surface $\tilde{A}$ can be related to the whole surface A_0 and the damage surface A_d as:

$$\tilde{A} = A_0 - A_d = A_0(1 - d) \tag{2}$$

Thus, from Equations (1) and (2), the apparent cohesive stress σ_i can be expressed as a function of the effective one $\tilde{\sigma}_i$ as:

$$\sigma_i = (1 - d)\tilde{\sigma}_i \tag{3}$$

Anyway, the displacement δ_i is the same for the apparent and effective behaviors of the interface, such as:

$$\delta_i = \frac{\sigma_i}{K_i} = \frac{\tilde{\sigma}_i}{K_i^0}, \tag{4}$$

Thus, introducing Eq.(4) into Eq.(3) leads to the expression of the apparent stiffness [1]:

$$K_i = (1 - d)K_i^0, \tag{5}$$

hence, the apparent cohesive stress yields:

$$\sigma_i = K_i^0(1 - d)\delta_i \tag{6}$$

[1] In case of zero thickness interface, the initial stiffness K_i^0 must tend towards infinity if the adhesion at the interface is perfect (K_i^0 is then qualified as a *penalty* stiffness) while K_i^0 will take a finite value in the case of a lack of cohesion of the interface which can be described from an initial damage surface A_d or, in a equivalent way, from an initial value of the damage variable d according to Eq.(5).

as shown in Figure 1.
According to Eq.(6), the softening behavior of the interface is related to the increase of the damage variable d while the apparent stress σ_i follow an exponential function:

$$\sigma_i(\delta_i) = \sigma_i^e e^{\phi_i(\delta_i^e - \delta_i)}, \tag{7}$$

where $\delta_i^e = \sigma_i^e / K_i^0$ [m] corresponds to the displacement at the end of the elastic regime and such as the cohesive energy G_{f_i} [J/m^2] verify $G_{f_i} = \int_0^\infty \sigma_i \, \mathrm{d}\delta_i$ which leads to:

$$\phi_i = \frac{2K_i^0 \sigma_i^e}{2K_i^0 G_{f_i} - (\sigma_i^e)^2} \tag{8}$$

According to Equations (6) and (7), the damage variable d can be expressed as:

$$d = 1 - \frac{\sigma_i^e}{K_i^0 \delta_i} e^{\phi_i \left(\frac{\sigma_i^e}{K_i^0} - \delta_i \right)} \tag{9}$$

Note that, according to the second law of the thermodynamics of irreversible processes, the evolution of the damage parameter is always positive ($\dot{d} \geq 0$, $d = max(d_{history})$).

To resume, for each fracture mode ($i = I$: Mode I and $i = II$: Mode II), the cohesive law of the interface is described with only three cohesive parameters: the initial stiffness K_i^0, the tensile or shear strength σ_i^e and the cohesive energy G_{f_i}. Thus, the pure Mode i cohesive law can be summarized as:

$$\sigma_i(\delta_i) = \begin{cases} K_i^0 \delta_i & \text{if } \delta_i \leq \delta_i^e \\ \sigma_i^e e^{\phi_i(\delta_i^e - \delta_i)} & \text{if } \delta_i^e \leq \delta_i < \delta_i^u \\ 0 & \text{if } \delta_i \geq \delta_i^u \end{cases} \tag{10}$$

where ϕ_i has been previously defined from Eq.(8) and δ_i^u corresponds to an upper cut-off of the displacement which can be introduced in order to indicate artificially the total failure of the interface (*i.e.*, $\sigma_i = 0$ and $d = 1$ for $\delta_i \geq \delta_I^u$) because the exponential function defined in Eq.(7) tends to $\sigma_i = 0$ asymptotically as a function of displacement δ_i. For instance, the upper cut-off of the displacement δ_i^u can be estimated from a percentage η of the strength σ_i^e that leads, in the case of an exponential softening, to:

$$\delta_i^u = \delta_i^e - \frac{1}{\phi_i} \ln(\eta) \tag{11}$$

3. Combined traction and shear loading: mixed-mode I+II CZM

3.1. Mixed-mode $I + II$

First CZMs (Hilleborg et al., 1976; Xu and Needleman, 1993; Camacho and Ortiz, 1996) have been developed for single mode fracture processes (*i.e.* for pure Mode I or pure Mode II fractures). Nevertheless, an interface is generally loaded in Mode I and in Mode II simultaneously (Zucchini and Lourenço, 2002) leading to *mixed-mode* $I + II$ fracture process. Therefore, various mixed-mode $I + II$ cohesive zone models have been proposed in order to describe such a complex fracture process (van den Bosch et al., 2006; Högberg, 2006; Snozzi and Molinari, 2013; Bisoffi-Sauve et al., 2019) which are mostly inspired by the pioneering model due to Camanho et al. (2003). The mixed-mode $I + II$ CZM proposed by Camanho et al. (2003) is formulated from the pure modes (Mode I and Mode II) cohesive laws (as detailed in the preceding Section) and leads to the expression of a mixed-mode cohesive law which has a form similar to those used for pure modes (Fig. 1), *i.e.*, characterized by an initial stiffness K^0_{I+II}, a strength σ^e_{I+II} (or a limit elastic displacement δ^e_{I+II}) and a cohesive energy $G_{f_{I+II}}$ as shown in Figure 2.
The mix of modes is obtained on the basis of a coupling parameter β corresponding to the ratio of the shear plane component of the displacement $\delta_{II_{I+II}}$ over the normal one $\delta_{I_{I+II}}$:

$$\beta = \frac{\delta_{II_{I+II}}}{\delta_{I_{I+II}}} = \tan(\alpha), \tag{12}$$

and from two criteria, the first one relating to the damage initiation and the second one corresponding to the interface failure.

Damage initiation criterion. It is assumed that the mixed-mode limit elastic stress σ^e_{I+II} corresponding to the damage onset and especially its Mode I and Mode II components, respectively noted as $\sigma^e_{I_{I+II}}$ and $\sigma^e_{II_{I+II}}$, must satisfy the quadratic stress criterion:

$$\left(\frac{\sigma^e_{I_{I+II}}}{\sigma^e_I}\right)^2 + \left(\frac{\sigma^e_{II_{I+II}}}{\sigma^e_{II}}\right)^2 = 1, \tag{13}$$

where, σ^e_I corresponds to the tensile strength in pure Mode I and σ^e_{II} is the shear strength in pure Mode II previously defined in Section 2.
On this basis, the initial stiffness of the Mode I and Mode II components

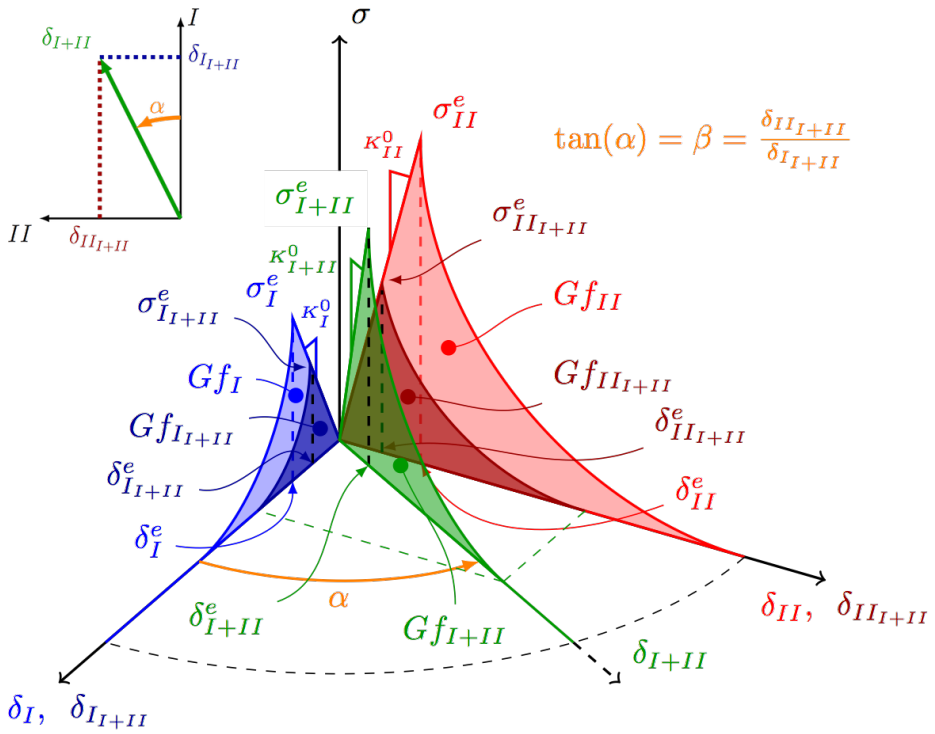

Figure 2: Mixed-mode cohesive law

of the mixed-mode being equal to the initial stiffness of the pure modes, *i.e.* $K^0_{I_{I+II}} = K^0_I$ and $K^0_{II_{I+II}} = K^0_{II}$, the quadratic stress criterion [Eq.(13)] can be rewritten in terms of displacements as:

$$\left(\frac{\delta^e_{I_{I+II}}}{\delta^e_I}\right)^2 + \left(\frac{\delta^e_{II_{I+II}}}{\delta^e_{II}}\right)^2 = 1 \tag{14}$$

Thus, using the relationships between the displacement δ_{I+II}, its Mode I and Mode II components ($\delta^e_{I_{I+II}}$ and $\delta^e_{II_{I+II}}$ respectively) and the coupling parameter β [Eq.(12)], the mixed-mode limit elastic displacement δ^e_{I+II} can be obtained from Equation (14) such as:

$$\delta^e_{I+II} = \delta^e_I\,\delta^e_{II}\sqrt{\frac{1+\beta^2}{(\delta^e_{II})^2 + (\delta^e_I\beta)^2}} \tag{15}$$

where δ^e_I and δ^e_{II} are the limit elastic displacements of the pure modes I and

II respectively [Eq.(10)]. Note that, according to Equation (15), a Mode I loading corresponding to a value of the coupling parameter $\beta = 0$ leads to $\delta^e_{I+II} = \delta^e_I$ while a Mode II loading, inducing $\beta \to \infty$, leads to $\delta^e_{I+II} = \delta^e_{II}$. Finally, the expression of the mixed-mode $I + II$ limit elastic stress σ^e_{I+II} yields:

$$\sigma^e_{I+II} = \delta^e_I \delta^e_{II} \sqrt{\frac{K_I^{0^2} + \beta^2 K_{II}^{0^2}}{\delta^{e^2}_{II} + \beta^2 \delta^{e^2}_I}} \tag{16}$$

Note that pure Mode I loading and pure Mode II loading correspond also to particular cases of Equation (16) insofar as $\sigma^e_{I+II} = \sigma^e_I$ for $\beta = 0$ and $\sigma^e_{I+II} = \sigma^e_{II}$ for $\beta \to \infty$ (Figure 3).

Failure criterion. The failure of an interface under mixed-mode loading is governed by the mixed-mode cohesive energy $G_{f_{I+II}}$. This cohesive energy can be expressed from the sum of its Mode I and Mode II components, $G_{f_{I_{I+II}}}$ and $G_{f_{II_{I+II}}}$ respectively, such as:

$$G_{f_{I+II}} = G_{f_{I_{I+II}}} + G_{f_{II_{I+II}}} \tag{17}$$

On this basis, a second criterion, named as *failure criterion* is necessary to estimate the value of mixed-mode cohesive energy $G_{f_{I+II}}$ (van den Bosch et al., 2006; Högberg, 2006; Snozzi and Molinari, 2013; Bisoffi-Sauve et al., 2019). This failure criterion is usually expressed through a power law of the Mode I and Mode II components of the cohesive energy, such as:

$$\left(\frac{G_{f_{I_{I+II}}}}{G_{f_I}}\right)^n + \left(\frac{G_{f_{II_{I+II}}}}{G_{f_{II}}}\right)^m = 1 \tag{18}$$

where G_{f_I} and $G_{f_{II}}$ are the cohesive energies relative to the pure modes I and II respectively (Section 2).
As a first approximation, a linear relationship is usually chosen from Eq.(18), *i.e.* $n = m = 1$ (Bisoffi-Sauve et al., 2019). Such a linear relationship ($n = m = 1$) will be also assumed in this study.
Let us express the Mode I and Mode II components of the mixed-mode cohesive energy as:

$$G_{f_{I_{I+II}}} = \Psi_{I_{I+II}}\, G_{f_I} \tag{19}$$

$$G_{f_{II_{I+II}}} = \Psi_{II_{I+II}}\, G_{f_{II}} \tag{20}$$

where $\Psi_{I_{I+II}}$ [1] and $\Psi_{II_{I+II}}$ [1] correspond respectively to the fractions of the *pure* Mode I and Mode II cohesive energies in the correspondent components of the mixed-mode cohesive energy. Therefore, according to Equations (19) and (20), the failure criterion defined in Eq.(18) yields :

$$\Psi_{I_{I+II}} + \Psi_{II_{I+II}} = 1 \tag{21}$$

Moreover, a given cohesive energy G_{f_i} can be expressed as the sum of the energy associated with the elastic part $G_{f_i}^e = \sigma_i^e \delta_i^e / 2$ and the one related to the softening part $G_{f_i}^{soft}$, i.e., $G_{f_i} = G_{f_i}^e + G_{f_i}^{soft}$. On this basis, the ratio of the *elastic* energy over the whole cohesive energy energy of a given mode must be maintained in the corresponding component of the mixed-mode such as:

$$\frac{G_{f_I}^e}{G_{f_I}} = \frac{G_{f_{I_{I+II}}}^e}{G_{f_{I_{I+II}}}} = {\phi_I}^e = cte \tag{22}$$

$$\frac{G_{f_{II}}^e}{G_{f_{II}}} = \frac{G_{f_{II_{I+II}}}^e}{G_{f_{II_{I+II}}}} = {\phi_{II}}^e = cte \tag{23}$$

Note that such ratio could be also expressed from the softening part of the cohesive behaviors. Finally, the parameters describing the elastic part of the cohesive behavior in pure modes (Section 2) and those of the mixed-mode (obtained from the damage initiation criterion) being known, the fraction of the Mode I cohesive energy in the mixed-mode cohesive energy $\Psi_{I_{I+II}}$ can be expressed, according to Equations (19) and (22), as:

$$\Psi_{I_{I+II}} = \frac{G_{f_{I_{I+II}}}}{G_{f_I}} = \frac{G_{f_{I_{I+II}}}^e}{G_{f_I}^e} = \frac{{\delta_{II}^e}^2}{{\delta_{II}^e}^2 + \beta^2 {\delta_I^e}^2} \tag{24}$$

while, according to Equations (20) and (23), the fraction of the Mode II cohesive energy in the mixed-mode cohesive energy $\Psi_{II_{I+II}}$ yields:

$$\Psi_{II_{I+II}} = \frac{G_{f_{II_{I+II}}}}{G_{f_{II}}} = \frac{G_{f_{II_{I+II}}}^e}{G_{f_{II}}^e} = \frac{\beta^2 {\delta_I^e}^2}{{\delta_{II}^e}^2 + \beta^2 {\delta_I^e}^2} \tag{25}$$

Note that, according to Equations (24) and (25), a Mode I loading corresponding to a value of the coupling parameter $\beta = 0$ leads to fractions of the Mode I and Mode II cohesive energies such as $\Psi_{I_{I+II}} = 1$ and $\Psi_{II_{I+II}} = 0$ and

hence, according to Equations (17) and (19), the mixed-mode cohesive energy is then equal to the Mode I cohesive energy $G_{f_{I+II}} = G_{f_I}$ as expected intuitively. Conversely, a Mode II loading inducing a coupling parameter $\beta \to \infty$ leads to fractions of the Mode I and Mode II cohesive energies such as $\Psi_{I_{I+II}} = 0$ and $\Psi_{II_{I+II}} = 1$ and so, according to Equations (17) and (20), to mixed-mode cohesive energy $G_{f_{I+II}} = G_{f_{II}}$, *i.e.*, the Mode II cohesive energy.

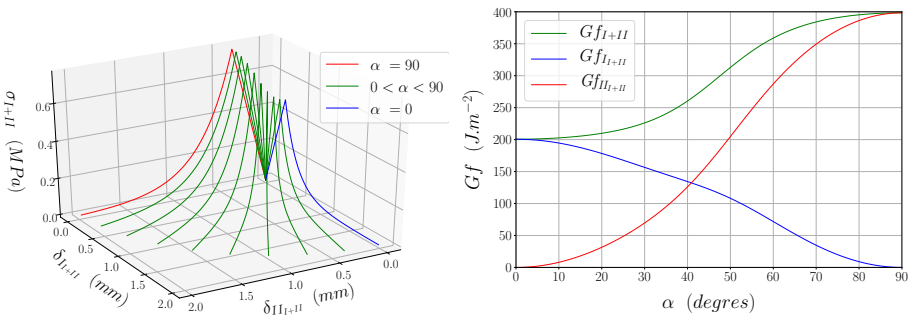

(a) (b)

Figure 3: Mixed-mode CZM as a function of the α angle: (a) Cohesive behavior *vs* α and (b) Mixed-mode cohesive energy and its Mode I and Mode II components *vs* α obtained for $G_{f_I} = 200J/m^2$ and $G_{f_{II}} = 400J/m^2$.

Figure 3(a) exhibits the response of the mixed-mode CZM when the interface is subjected to a monotonically rising displacement δ_{I+II} up to the ultimate displacement δ^u_{I+II} according to various α angles (Fig. 2) ranged between 0 and 90 degrees. It can be observed from Figure 3(b) that mixed-mode cohesive energy $G_{f_{I+II}}$ (Equation 17) increases from the Mode I cohesive energy $G_{f_{I+II}} = G_{f_{I_{I+II}}} = G_{f_I}$ when the interface is loaded according to $\alpha = 0\,\text{deg}$ (for this example, the value G_{f_I} has been fixed to $200J/m^2$) to the Mode II cohesive energy when $\alpha = 90\,\text{deg}$, i.e., $G_{f_{I+II}} = G_{f_{II_{I+II}}} = G_{f_{II}}$ with here $G_{f_{II}} = 400J/m^2$.

3.2. Influence of the mixed-mode coupling on the dissipated energy

As previously mentioned, the quasi-brittle damage being caused by extension, the dissipated energy is expected to be different if the interface is firstly loaded in pure traction then in pure shear and conversely. A way of studying the behavior of a coupled cohesive zone law is to analyze the dissipated energy under combined normal and shear loading as proposed by van

den Bosch et al. (2006).
In a first case, the interface is loaded in the direction I (*i.e.*, $\alpha = 0\,\text{deg}$) up to a displacement $\delta^*_{I_{I+II}}$ whose value is a percentage of the ultimate one δ^u_I then, $\delta^*_{I_{I+II}}$ is kept constant and a displacement is applied in the direction II up to the corresponding ultimate one $\delta_{II_{I+II}} = \delta^u_{II}$ (Fig. 4(a)). This first case of non-proportional loading is applied for various ratio $\delta^*_{I_{I+II}}/\delta^u_I$ ranged between 0 and 1.
In the second case (Fig. 4(b)), the interface is firstly loaded in the direction II (*i.e.*, $\alpha = 90\,\text{deg}$) up to a displacement $\delta^*_{II_{I+II}}$ corresponding to a percentage of the ultimate one δ^u_{II} then, $\delta^*_{II_{I+II}}$ is kept constant and a displacement is applied in the direction I up to the ultimate one $\delta_{I_{I+II}} = \delta^u_I$. As for the first case, the second loading case is applied for various ratio $0 \leq \delta^*_{II_{I+II}}/\delta^u_{II} \leq 1$.
The mixed-mode energy $G_{f_{I+II}}$ dissipated during both cases as well as the

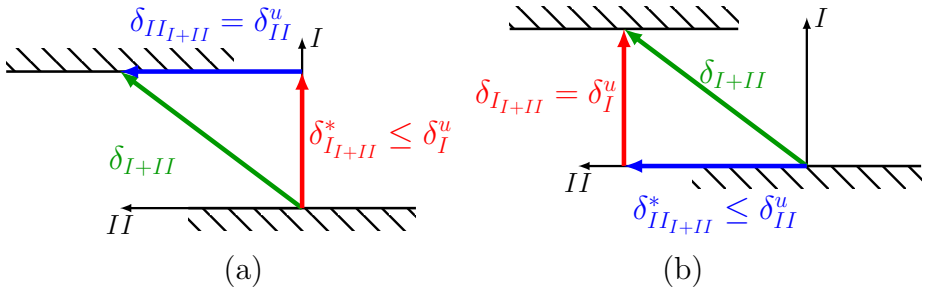

Figure 4: Loading sequence to study the influence of the coupling parameters on the work-of-separation: as proposed by van den Bosch et al. (2006)

Mode I and Mode II components of this energy, $G_{f_{I_{I+II}}}$ and $G_{f_{II_{I+II}}}$ respectively, are plotted in Figure 5 as a function of the ratio $\delta^*_{I_{I+II}}/\delta^u_I$ relative to the first case (Fig. 5(a)) and $\delta^*_{II_{I+II}}/\delta^u_{II}$ corresponding to the second case (Fig. 5(b)).
In the first case (Fig. 5(a)), as expected, the dissipated energy $G_{f_{I+II}} = G_{f_{II_{I+II}}} = G_{f_{II}}$ when the ratio $\delta^*_{I_{I+II}}/\delta^u_I = 0$ which corresponds to a pure shear loading of the interface while, $G_{f_{I+II}} = G_{f_{I_{I+II}}} = G_{f_I}$ when $\delta^*_{I_{I+II}}/\delta^u_I = 1$ corresponding to pure traction loading. Moreover, the dissipated energy decreases monotonically as a function of the ratio $\delta^*_{I_{I+II}}/\delta^u_I$ from $G_{f_{II}}$ to G_{f_I} exhibiting a consistent physical behavior.
In the second case (Fig. 5(b)), the dissipated energy $G_{f_{I+II}}$ increases monotonically as a function of the ratio $\delta^*_{II_{I+II}}/\delta^u_{II}$ from $G_{f_{I+II}} = G_{f_{I_{I+II}}} = G_{f_I}$ when $\delta^*_{II_{I+II}}/\delta^u_{II} = 0$ which corresponds to pure traction loading of the inter-

face, to $G_{f_{I+II}} = G_{f_{II_{I+II}}} = G_{f_{II}}$ when $\delta^*_{II_{I+II}}/\delta^u_{II} = 1$ corresponding a pure shear loading of the interface.
As a conclusion, the monotonous evolutions of the mixed-mode dissipated energy observed from both loading cases in Figures 5(a) and 5(b) seems to be consistent with the expected behavior of a quasi-brittle interface.

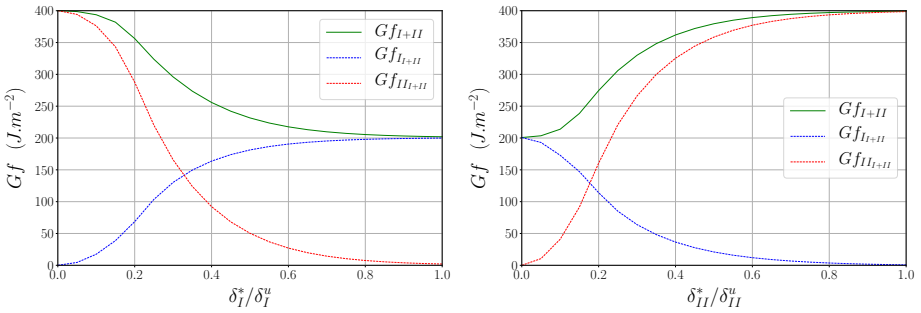

(a) (b)

Figure 5: Energy dissipated from non proportionnal loading (with $Gf_I = 200J/m^2$ and $Gf_{II} = 400J/m^2$)

In the following part, cases of combined compression and shear loadings applied to the interface are studied. In these cases, friction effect strongly influences the mechanical response of the interface and hence, a coupling between frictional and Mode II cohesive behaviors based on an estimation of the effective frictional area is proposed.

4. Combined compression and shear loading: Frictional Mode II CZM

4.1. Monotonically loading

When the interface is subjected to shear and compression loading, the contribution of the friction must be taken into account to describe accurately the interface behavior. As mentioned in Introduction, in most models, the *full* friction stress is usually considered from the onset of cohesive behavior and leads to consider that the friction effect takes place while the cohesive capacity of the interface is still intact. To overcome this physical inconsistency, several authors (Chaboche et al., 1997; Snozzi and Molinari, 2013; Spring and Paulino, 2015; D'Altri et al, 2018) introduce, in their CZM, a phenomenological progressive rising of the friction stress as a function of

the shear plane displacement which allow a better description of experimental stress-displacement responses. Nevertheless, assuming a friction stress depending of shear plane displacement is not physically based because friction stress is expected to depend only on normal stress, on friction coefficient and on the surface area on which acts the friction effect. Thus, as proposed by Raous and Monerie (2002), Acary and Monerie (2006) and Alfano and Sacco (2006), a coupling based on the damage part of the interface on which the frictional phenomenon can physically act appears more relevant.
In the following, taking inspiration from these latter works, a frictional Mode II cohesive zone model founded on a physically based coupling of cohesive and frictional behaviors is proposed. The coupling is here introduced from the damage variable, single internal variable of the model, which gives an estimate of the effective damage area of the interface.

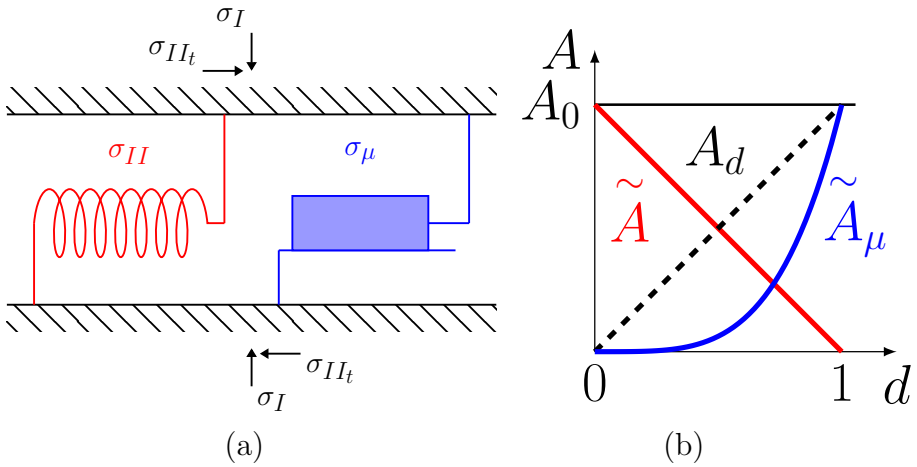

Figure 6: Combined compression and shear loading, based on apparent stresses: (a) rheological model, and on effective stresses: (b) evolution of effective areas against interface area A_0

Let us consider the rheological model shown in Figure 6(a) which consists in a cohesive spring and a friction pad in parallel in order to describe the interface mechanical behavior. According to this rheological model, the shear stress σ_{II_t} can be expressed as the sum of the cohesive stress σ_{II} and the frictional stress σ_μ:

$$\sigma_{II_t} = \sigma_{II} + \sigma_\mu \tag{26}$$

Note that all stresses in Eq.(26) correspond to *apparent* stresses, *i.e.*, stresses

acting on the whole surface of the interface A_0.
Moreover, according to Eq.(1), the apparent cohesive stress σ_{II} [Eq.(26)] can be expressed from the effective cohesive stress $\tilde{\sigma}_{II}$ acting on the effective cohesive area $\tilde{A} = A_0(1-d)$ and yields:

$$\sigma_{II} = \tilde{\sigma}_{II}\frac{\tilde{A}}{A_0} = \tilde{\sigma}_{II}(1-d) = K_{II}^0(1-d)\delta_{II} \tag{27}$$

An example of the cohesive stress σ_{II} *vs* δ_{II} behavior is plotted in Figure 7 (red curve).
In the same way, the apparent frictional stress σ_μ [Eq.(26)] can be expressed, according to Eq.(1), from the effective cohesive stress $\tilde{\sigma}_\mu$ acting on the effective frictional area $\tilde{A}_\mu$ such as:

$$\sigma_\mu = \tilde{\sigma}_\mu \, \frac{\tilde{A}_\mu}{A_0} \tag{28}$$

where the effective frictional stress $\tilde{\sigma}_\mu$ is defined, according to the Coulomb's law, as:

$$0 \leq |\tilde{\sigma}_\mu| \leq \tilde{\sigma}_{\mu_c} = \mu \, \sigma_I \tag{29}$$

where μ is the friction coefficient and $\tilde{\sigma}_{\mu_c} = \mu \, \sigma_I$ corresponds to the shear sliding resistance.
Regarding the effective frictional area $\tilde{A}_\mu$ [Eq.(28)], it is assumed that this area corresponds to a part or all of the damage area $A_d = d \, A_0$ through the function $f(d) = d^p$ with $p \geq 1$, as shown in Fig. 6(b):

$$\tilde{A}_\mu = f(d)A_0 = d^p A_0 \tag{30}$$

Indeed, at the onset of interface damage (*i.e.*, $d \simeq 0$), combination to both compression and shear loading leads to extension (strain) approximately oriented at 45° with respect to the interface plane which, in a case of a quasi-brittle material, generates microcracks oriented perpendicularly to the extension direction. Due to this preferential orientation of microcracks, the shear loading tends to open the microcraks and consequently to cancel the friction effects on the damage area (for $d \simeq 0$, $\tilde{A}_\mu \simeq 0$ and so $\sigma_\mu \simeq 0$). Then, with the increase of interface damage (*i.e.*, $0 < d < 1$), the number of microcracks increases ($0 < A_d < A_0$) and the microcracks progressively coalesce towards a main crack oriented in parallel to the interface plane on which compression and shear loadings act simultaneously. This progressive change in the orientation of cracking (from 45° to 0° with respect to the interface plane) coupled

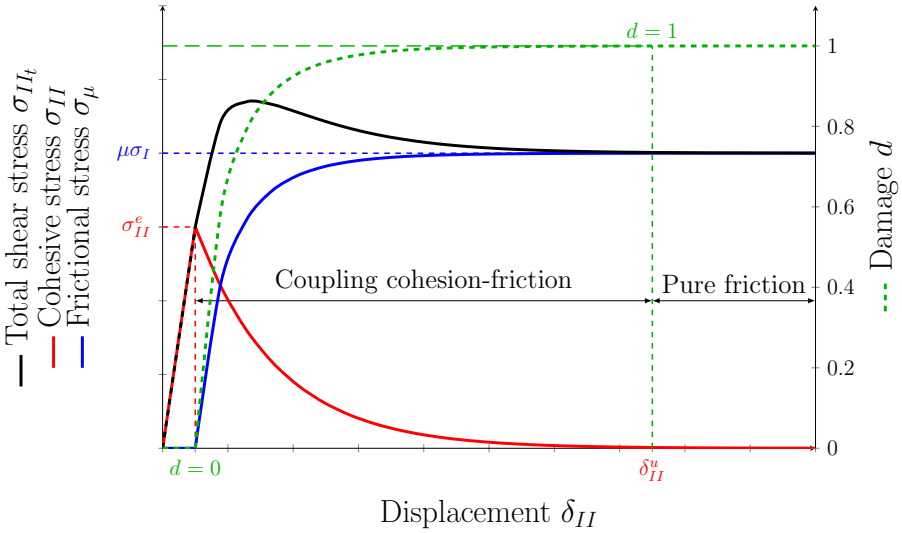

Figure 7: Total shear stress *vs* shear plane displacement response obtained from FCZM and its frictional and cohesive components.

to the increase of damage area lead to an increase of the effective frictional area $\tilde{A}_\mu$ (but $\tilde{A}_\mu \leq A_d$) and hence of the frictional stress σ_μ. Finally, when the failure of interface occurs (*i.e.*, $d = 1$), the effective frictional area $\tilde{A}_\mu$ equals the damage area A_d and both correspond to the whole interface area A_0 which leads to an apparent frictional stress such as: $\sigma_\mu = \mu\, \sigma_I$. Note that the function $f(d) = d^p$ which corresponds to the ratio of the effective frictional area $\tilde{A}_\mu$ over the damage area A_d must correspond to a concave form as shown in Fig. 6(b) since the effective frictional area must not exceed the damage one ($\tilde{A}_\mu \leq A_d$). Nevertheless, another form of concave function could be used to describe $f(d) = \tilde{A}_\mu / A_d$ instead of $f(d) = d^p$ with $p \geq 1$.

Thus, according to Eqs.(29) and (30), the apparent frictional stress σ_μ [Eq.(28)] yields:

$$0 \leq |\sigma_\mu| \leq \sigma_{\mu_c}(d) = f(d)\, \mu\, \sigma_I \tag{31}$$

where $\sigma_{\mu_c}(d)$ corresponds to the *apparent* friction sliding threshold which increases as a function of the damage variable d as shown in Figure 7 (blue curve) and leads to the classical value of the sliding stress $\sigma_{\mu_c} = \mu\, \sigma_I$ when $d = 1$, *i.e.* when the interface is totally failed. Note that, according to Eq.(31), the apparent friction sliding stress $\sigma_{\mu_c}(d)$ can be also expressed as $\sigma_{\mu_c}(d) = \mu(d)\, \sigma_I$ where $\mu(d) = \mu\, f(d) = \mu\, d^p$ can be seen as the apparent

friction coefficient evolving as a function of the damage level.

Finally, according to Eqs.(27) and (28), the apparent shear stress σ_{II_t} [Eq.(26)] yields:

$$\sigma_{II_t} = K_{II}^0(1-d)\delta_{II} + \sigma_\mu \tag{32}$$

where the frictional stress $|\sigma_\mu| \leq \sigma_{\mu_c}(d)$ and where $\sigma_{\mu_c}(d) = d^p\ \mu\ \sigma_I$ corresponds to the apparent sliding resistance. According to Eq.(32), an example of the shear stress σ_{II_t}, resulting from the sum of the cohesive stress σ_{II} and of the shear one σ_μ, is plotted in Figure 7 (black curve). The shape of the obtained σ_{II_t} *vs* δ_{II} response is in agreement that those usually observed experimentally for interfacial failure and describes a smooth transition from a cohesive zone to a pure frictional contact zone.

Moreover, regarding the general shear behavior of the interface given by Eq.(32), when the apparent frictional stress $|\sigma_\mu| < \sigma_{\mu_c}(d)$, the interface displacement is blocked (due to blocking on the effective frictional area $\tilde{A}_\mu$) and hence the cohesive part is no longer loaded (but the cohesive stress σ_{II} remains its value before blocking). Conversely, when $|\sigma_\mu| = \sigma_{\mu_c}(d)$, the interface displacement is possible due to sliding on $\tilde{A}_\mu$ and both cohesive and frictional parts are loaded. This consequences of the rheological model (cohesive spring and a friction pad in parallel as shown Fig. 6(a)) are detailed in the following section from cyclically loading of the interface.

4.2. Response obtained under cyclic loading

In this section, the simulation of a cyclic loading test (obtained from an analytical computation) is carried out to show, from a qualitative point of view, the main features of the proposed constitutive model. The cyclic shear response of the FCZM model is shown in Figure 8. The interface is subjected to a constant compressive normal stress and to tangential cyclic stress through an imposed tangential displacement. Figure 8 shows the evolution of total shear stress $\sigma_{II_t} = \sigma_{II} + \sigma_\mu$ as a function of shear displacement δ_{II} while the evolution of damage variable d is plotted on the secondary axis. The cyclic path is characterized by two loading-unloading cycles (cycle 1: *ABCD* and cycle 2: *EFG)*. In order to ensure an easier description of the loading-unloading behavior, the damage level is kept constant during both cycles.

At the onset of the loading, as long as the cohesive shear stress is lower than the shear strength ($\sigma_{II} < \sigma_{II}^e$), the model remains in the elastic domain (phase *OO'*) and damage variable $d = 0$. When the shear strength σ_{II}^e is

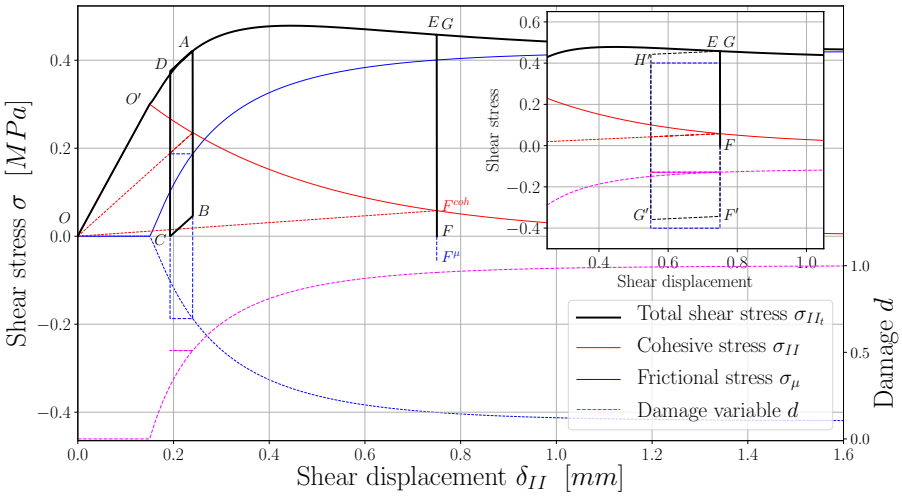

Figure 8: FCZM response expected in the case of two load-unload cycles performed during an unilateral shear test under compression. Inserted graph: example of expected response from a bilateral shear test.

reached (point *O'*), the cohesive stress σ_{II} decreases following the softening exponential law [Eq. (7)] and frictional stress σ_{μ} begins to increase according to the rising of damage variable d, *i.e.*, $\sigma_{\mu} = \sigma_{\mu_c}(d)$. Note that during the phase *O'A* the imposed shear displacement is positive $\dot{\delta}_{II} > 0$ which implies that cohesive stress as well as the frictional one are positive.

Cycle *ABCD-unilateral shear test*: From point A, the displacement δ_{II} is no longer imposed and the interface is unloaded under the sole effect of the cohesive part (this situation corresponds to the realization of an unilateral shear test). This induces a change in the sign of frictional stress ($\sigma_{\mu} < 0$) while the cohesive one remains positive. The fact that $\sigma_{\mu} = -\sigma_{\mu_c}(d)$ leads to a vertical jump of the total shear stress up to point B such as $|\Delta\sigma_{II_t}| = 2\sigma_{\mu_c}(d)$ while the value of the cohesive stress remains constant. From point B, a decrease of the total shear stress is observed up to point C (with $\dot{\delta}_{II} < 0$) which corresponds to a sliding phase of the interface since the value of the cohesive stress is greater than the one of the frictional one $\sigma_{II} > |\sigma_{\mu}|$ where $\sigma_{\mu} = -\sigma_{\mu_c}(d)$ with $d = cte$. The slope of the BC part corresponds to the stiffness of the cohesive spring $K_{II} = K^0_{II}(1-d)$. At point C, the total shear stress value is equal to zero which corresponds to the balance between cohesive and frictional residual stresses such as $\sigma_{II} = -\sigma_{\mu} = -\sigma_{\mu_c}(d)$.
From point C, the displacement δ_{II} is again imposed with $\dot{\delta}_{II} > 0$ and then

the value of frictional stress becomes again positive. Thus, the change in loading direction again induces a jump of the total shear stress up to the point D whose magnitude corresponds to $|\Delta\sigma_{II_t}| = 2\sigma_{\mu_c}(d)$ (since the value of σ_μ changes from $-\sigma_{\mu_c}(d)$ to $\sigma_{\mu_c}(d)$) then an interface sliding occurs from the point D to the point A since the value of the cohesive stress becomes greater to the one of the frictional stress is $\sigma_{II} > \sigma_\mu$ with $\sigma_\mu = \sigma_{\mu_c}(d)$. The slope of the part DA corresponds to the stiffness of the cohesive part $K_{II} = K_{II}^0(1-d)$.
Thus, the cycle $ABCD$ exhibits an hysteresis effect induced by the interface sliding along the part BC and DA and associated dissipated energy from friction effect.

Then, from point A a monotonically loading (i.e., $\dot{\delta_{II}} > 0$ where δ_{II} is imposed) is carried out from point A to point E. The branch AE highlights the rising of damage variable which leads to a softening of the cohesive law and an increase of the frictional stress.

Cycle *EFG-unilateral shear test*: From point E, the displacement δ_{II} is no longer imposed again and, as from point A, the interface is unloaded according to an unilateral shear test in which the displacement can be also induced by the cohesive part of the model. This unloading leads to a change in the sign of frictional stress ($\sigma_\mu < 0$) and induces a *theoretical* vertical jump of the total shear stress such as $|\Delta\sigma_{II_t}| = 2\sigma_{\mu_c}(d)$ while the value of the cohesive stress remains constant and positive.

However, the unloading being carried out under the sole effect of the cohesive spring (unilateral shear test), the fact that the cohesive stress is lesser than the frictional one leads only to a jump of the total shear stress up to $\sigma_{II_t} = 0$ (point F) which corresponds to residual stresses such as $\sigma_\mu = -\sigma_{II}$ with $|\sigma_\mu| < \sigma_{\mu_c}(d)$ meaning the blockage of the interface.
If the interface is then re-loaded from point F ($\dot{\delta_{II}} > 0$ where δ_{II} is imposed), the value of frictional stress becomes again positive and leads to a jump of the total shear stress up to point G induced by the increase of the frictional stress magnitude up to the value $\sigma_{\mu_c}(d)$ (while the cohesive stress value remains constant) from which the interface can slide again but with an increase of the damage variable d.
Thus, from an unilateral shear test, when the cohesive stress becomes lesser than the frictional one, an unloading-loading cycle takes place without hysteresis effect because the sole effect of the cohesive part is not sufficient to induce a sliding of the interface. Conversely, when the cohesive stress is greater than the frictional one, an unloading-loading cycle will exhibit an

hysteresis effect (cycle $ABCD$).

Cycle *EF'G'H'-bilateral shear test* (graph inserted in Fig. 8): Now consider that the unloading is carried out from point E through a bilateral shear test rather than an unilateral one, i.e., the shear displacement is imposed for $\dot{\delta_{II}} < 0$, the total shear stress exhibits effectively the *theoretical* vertical jump of magnitude $|\Delta\sigma_{II_t}| = 2\sigma_{\mu_c}(d)$ up to the point F'. From this point, the interface is then able to slide since the frictional stress is equal $\sigma_\mu = -\sigma_{\mu_c}(d)$ and the interface exhibits a stiffness corresponding to the one of the cohesive part $K_{II} = K_{II}^0(1-d)$ (part $F'G'$). From point G', the interface is re-loaded ($\dot{\delta_{II}} > 0$) and, as previously explained, the reverse of the loading leads to a change in the sign of frictional stress ($\sigma_\mu > 0$) inducing a jump of the total shear stress such as $|\Delta\sigma_{II_t}| = 2\sigma_{\mu_c}(d)$ up to point H' (while the cohesive stress remains constant and positive) from which the interface is again able to slide (since $\sigma_\mu = \sigma_{\mu_c}(d)$) up to point G, exhibiting the stiffness $K_{II} = K_{II}^0(1-d)$. Note that the cycle $EF'G'H'$ exhibits an hysteresis effect linked to the sliding of the interface along the parts $F'G'$ and $H'G$ and the associated dissipated energy.

5. Estimation of cohesive and frictional parameters in the context of masonry : block-mortar interface

Frictional Cohesive Zone Model described in the previous sections is applied in the following in the context of masonry where the knowledge of the mechanical behavior of interface between stone block and joint mortar is particularly relevant with regard to the accurate description of the mechanical behavior of masonry.

FCZM parameters introduced in Sections 3 and 4 are identified on the interface between limestone blocks and hydraulic lime mortar (NHL 3.5)[2]. In the following, the first part presents the main mechanical properties of the masonry constituents: limestone blocks and mortar. Then, a direct tensile test carried out on a duo of limestone blocks assembled by one mortar joint and leading to an estimation of the FCZM Mode I cohesive parameters (K_I^0 $[N/m^3]$, σ_I^e $[N/m^2]$ and G_{f_I} $[J/m^2]$) is presented. Finally, a shear test performed on a triplet of limestone blocks assembled by two mortar joints is described. This test allows estimating the Mode II cohesive parameters

[2]Limestone blocks and hydraulic lime mortar (NHL 3.5) are traditionally used in western region of France for small residential buildings, buildings, churches and bridges

Designation	Quantity	Symbol	Value (CV)	Unit
Limestone	Youngs modulus	E_b	11.1 (15%)	GPa
blocks	Compressive strength	σ_{c_b}	9.5 (26%)	MPa
Hydraulic	Youngs modulus	E_m	*3.95*	GPa
lime	Compressive strength	σ_{c_m}	1.9 (14%)	MPa
mortar	Flexural strength	σ_{f_m}	0.6 (6%)	MPa

Table 1: Mechanical characteristics of limestone blocks and hydraulic lime mortar. The Young's modulus of lime mortar E_m has been estimated by Bisoffi-Sauve (2016) for the same mixture of lime mortar.

(K^0_{II} $[N/m^3]$, σ^e_{II} $[N/m^2]$ and $G_{f_{II}}$ $[J/m^2]$) and frictional parameters (μ [1] and p [1]).

5.1. Characterization of constituents materials

Limestone blocks. The limestone used in this study is typical of the south-west of France and stem from *Pierres de Frontenac* stone quarry. Their compressive properties are determined, according to EN 1926 (2006), from 20 specimens. The blocks tested of nominal dimensions of $100\times100\times100$ mm^3 are positioned between steel plates and 4 extensometers attached directly to the specimen allow to measure strains. Average compressive strength and Youngs modulus obtained from the compression tests are reported in Table 1.

Mortar joints. The lime mortar used in this study is composed of sand, hydraulic lime (NHL 3.5) and water. Proportions by volume of the lime, sand and water in the mixture are estimated by a master stonemason on the basis to 1 part of lime and 3 parts of sand. After that, water is added in the mixture until reaching desired traditional workability. Finally, measured proportions in grams are: 1 (NHL3.5): 6.5 (sand 0-2 [mm]): 1.5 (water). Flexural strength and compressive strength were obtained according to EN 1015-11 (2007) on 8 specimens ($4 \times 4 \times 16$ cm^3). Average flexural strength and compressive strength obtained from lime mortar are reported in Tab. 1.

5.2. Estimation of Mode I cohesive parameters: direct tensile test

5.2.1. Experimental set-up

The cohesive parameters characterizing the Mode I fracture behavior of a block-mortar interface are usually estimated from a direct tensile test (van

Mier, 1996; van der Pluijm, 1999; Almeida et al., 2002; Bisoffi-Sauve, 2016; Sandoval and Arnau, 2017; Bisoffi-Sauve et al., 2019). Despite some differences between the tensile tests proposed in the literature, they can be categorized as a function of their boundaries conditions: rotating supports or fixed supports. Experimental set-up using fixed supports leads to a higher value of the cohesive energy and the tensile strength compared to the one using rotating supports insofar as fixed supports limit flexure effects and induce a more uniform damage of the interface (van Mier, 1996). On this basis, an experimental set-up using fixed supports is chosen in this study to characterize the block-mortar interface in Mode I (Bisoffi-Sauve, 2016; Bisoffi-Sauve et al., 2019).

According to experimental set-up proposed Bisoffi-Sauve et al. (2019), duo of limestone blocks ($10 \times 10 \times 7$ cm^3) assembled by one mortar joint ($10 \times 10 \times 0.7$ cm^3) are directly glued (epoxy resin) inside steel boxes fixed on universal testing machine of 100 kN maximum load capacity thus restricting rotations of blocks during tensile test as shown in Figure 9(b). Experiments are controlled by the opening rate of the mortar joint obtained from the average of displacements measured by four extensometers located on each side of the sample (in the vicinity of corners as proposed by van der Pluijm, 1999) (Figure 9(a)), imposing a opening displacement at constant velocity (0.3 μm/min). In order to limit long term mechanical effects, the opening rate is gradually increased in the post-peak regime to reach 100 μm/min at the end of the test.

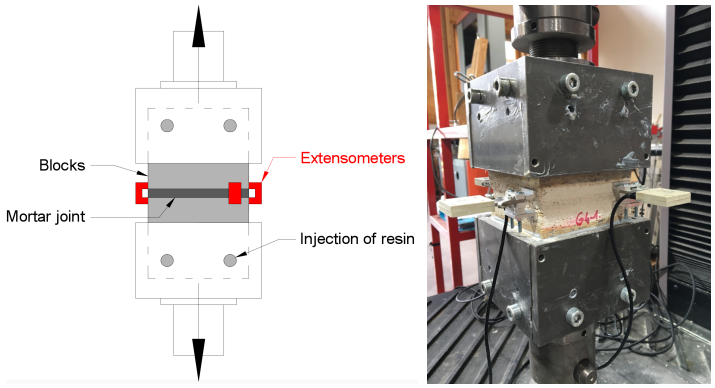

(a) (b)

Figure 9: Tensile test setup: (a) location of extensometers measuring the opening displacement of the mortar joint and (b) picture of test setup

5.2.2. Estimation of Mode I cohesive parameters

As usually observed from direct tensile test, the failure of mortar joint is mainly located at the block-mortar interface. As a consequence, if the tensile stress obtained from the ratio of the tensile load over the specimen nominal cross section is characteristic of the tensile stress applied on the interface, the average displacement measured from the extensometers does not reflect the single opening of the interface. Indeed, as the extensometers are fixed on stone blocks in the immediate vicinity of the joint as shown from Fig. 9(a), the measured displacement value also includes the extension of the mortar joint and, to a lesser extent, the extension of limestone. Thus, knowing the Young's moduli of lime mortar (3.95 GPa, Bisoffi-Sauve, 2016) and limestone (11.1 GPa, Tab. 1), the interface opening is estimated from the average displacement measured from the extensometers in substracting the limestone and joint extensions and this for all values of the tensile stress.
Figure 10(a) exhibits experimental tensile stress *vs* interface opening responses obtained from the tensile test. As previously shown in several studies (van der Pluijm, 1999; Bisoffi-Sauve, 2016; Sandoval and Arnau, 2017; Bisoffi-Sauve et al., 2019), the initial elastic response is followed after the peak stress by a strain negative hardening phase characteristic of the quasi-brittle fracture behavior of the mortar joint and especially the fracture energy required to completely separated the two limestone blocks.

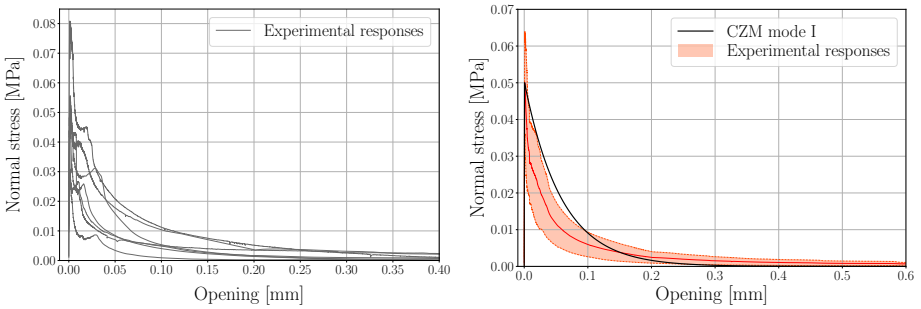

(a) (b)

Figure 10: Direct tensile test results: (a) experimental $\sigma_I - \delta_I$ responses and (b) Mode I cohesive behavior obtained from Eq.(10) compared to the average experimental response more or less one standard deviation

The Mode I cohesive parameters are directly estimated from the tensile stress *vs* opening displacement responses plotted in Fig.10(a). The initial stiffness K_I^0 is estimated from a linear regression of the elastic regime before

Designation	Quantity	Symbol	Value	Unit
Mode I	Initial stiffness	K_I^0	1.21×10^{11}	Pa/m
	Maximum stress	σ_I^e	0.05	MPa
	Cohesive energy	Gf_I	3	J/m^2
Mode II	Initial stiffness	K_{II}^0	2.82×10^{11}	Pa/m
	Maximum stress	σ_{II}^e	0.27	MPa
	Cohesive energy	Gf_{II}	206	J/m^2
Frictional parameters	Frictional coefficient	μ	0.81	1
	Exponent of $f(d)$ function	p	11.0	1

Table 2: FCZM parameters obtained from experimental campaign

the peak stress, the maximum tensile stress σ_I^e is directly obtained from the experimental peak stress while the cohesive energy G_{f_I} is estimated from the area under the $\sigma - \delta$ response. The average of each cohesive parameters is given in Table 2. On this basis and according to Eq.(10), the Mode I cohesive response corresponding to these average parameters is plotted in Figure 10(b) and exhibits a fairly good agreement with the average experimental tensile stress-opening displacement response more or less one standard deviation.

5.3. Mode II characterization: triplet shear test

In literature, there is a large variety of experimental setups allowing combined compression and shear loadings. Among the different proposed setups, one can note (i) the direct shear test used by van der Pluijm (1999) (Fig. 11(a)), (ii) the couplet test (Fig. 11(b)) and (iii) the triplet test requested by EN 1052-3 (2007) shown in Fig. 11(c). The first test (van der Pluijm, 1999) requires very stiff supports to prevent flexure effects while the second one (Lourenço and Ramos, 2004; Abdou et al., 2006) is not symmetrical and can lead to a non homogeneous loading on the mortar joint if the boundary conditions are not perfectly controlled. On this basis, the triplet test appears as the most appropriate insofar as it is symmetric and does not require excessively stiff supports. Furthermore, the simultaneous test of two mortar joints, which may exhibit scattered mechanical properties, leads to the mechanical characterization of a *single* joint whose response corresponds to the average responses of the two joints (Zhang et al., 2008).

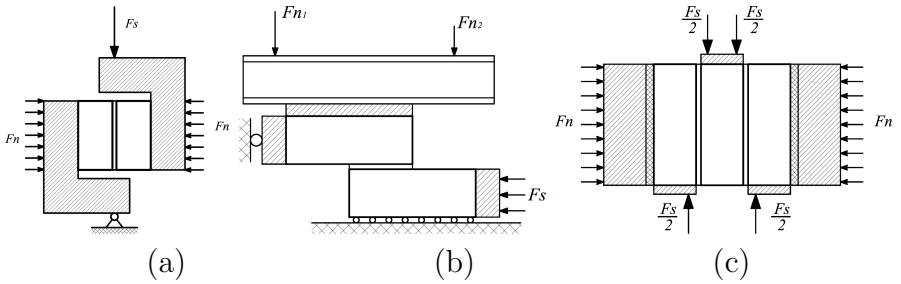

Figure 11: Different types of combined compression and shear test setups: (a) van der Pluijm (1999), (b) couplet test and (c) triplet test (Figure extracted from Lourenço and Ramos, 2004)

5.3.1. Experimental setup

The triplet test is chosen in this study to characterize the frictional and Mode II cohesive properties; this test can exhibits more or less pronounced parasitic loadings. Indeed, a bending loading may appear on the sample especially if the blocks dimension is not sufficient in the direction of the transverse loading (shear loading) as well as a parasitic torsion loading can act on the sample due to the flatness defects of the reference face (supported face) of sample. Improvements of the triplet test (EN 1052-3, 2007) have been recently proposed by Bisoffi-Sauve et al. (2019). The first one, inspired by the EN 13733 (2002) test, is to fix the two end blocks by means of clamping rods in order to prevent bending loading (Fig. 12(b)). The second improvement consists in the modification of one of the supports by the introduction of a degree of freedom in rotation with respect to the axis perpendicular to the joints in order to adapt to flatness defects of the sample supported face.
According to experimental set-up proposed by Bisoffi-Sauve et al. (2019), triplet of limestone blocks ($10 \times 10 \times 10$ cm^3) assembled by two mortar joints ($10 \times 10 \times 0.7$ cm^3) are initially submitted to a compression loading leading to a normal stress on the mortar joint and then fixed on universal testing machine of 100 kN maximum load capacity at the end blocks. Three normal stress levels are applied on the mortar joint: 0.4 MPa, 0.6 MPa and 0.8 MPa. Specimens are tested by imposing a vertical displacement to the central block leading to shearing of the mortar joints. Experiments are controlled by the shear plane displacement rate of the mortar joints obtained from the average of displacements measured by four extensometers located on both sides of the sample in the immediate vicinity of the joints (Fig. 12(a)). At the onset of the test, the velocity of the average shear plane displacement is imposed

to 0.5 μm/min then is gradually increased in the post peak regime to reach 100 μm/min at the end of the test.

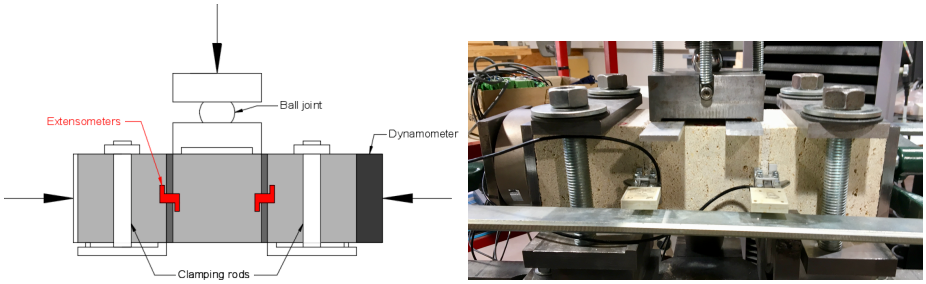

(a) (b)

Figure 12: Combined compression and shear test setup: (a) position of extensometers and (b) picture of the triplet test

5.3.2. Estimation of frictional and Mode II cohesive parameters

As previously observed from tensile test, shear test exhibits also failures mainly located of the block-mortar interface. Thus, the shear plane displacement corresponding to the interface needs to be estimated from the average displacement measured from the four extensometers by substracting the contributions of the mortar joint and of the limestone knowing the shear moduli of materials ($G = E/[2(1+\nu)]$ with a Poisson's ratio of 0.2). Moreover, the shear stress is obtained by dividing the vertical load applied on the central block by the nominal cross section of both joints while the normal stress is estimated from the compression load divided by the nominal cross section of one joint. As the effective section of the joints gradually decreases according to the shear plane displacement, the values of the shear and normal stresses are updated as a function the shear displacement value.

Six to seven specimens have been tested for each normal stress level (0.4, 0.6 and 0.8 MPa). From the experimental shear stresses *vs* shear displacement responses of the block-mortar interface (i.e., σ_{II_t} *vs* δ_{II}) obtained for each normal stress level, the average shear stress and the standard deviation of this one $\Delta\sigma_{II_t}$ are computed as a function of the shear plane displacement δ_{II} and are plotted in Figure 13(a): blue color for experimental ($\sigma_{II_t} \pm \Delta\sigma_{II_t}$) *vs* δ_{II} response obtained for $\sigma_N = 0.4$ MPa, green color for $\sigma_N = 0.6$ MPa and red color for $\sigma_N = 0.8$ MPa.

First of the mechanical parameters estimated from the experimental re-

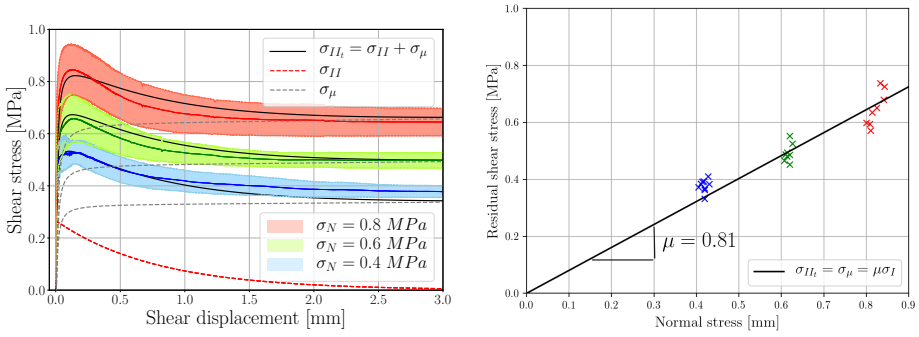

(a) (b)

Figure 13: Experimental results obtained from improved triplet shear tests: (a) average experimental shear stress *vs* shear displacement responses of the block-mortar interface and (b) estimation of friction coefficient linear regression

sponses plotted in Fig. 13(a), the friction coefficient μ is obtained from a linear regression of the residual stress (*i.e.*, the constant stress observed for large shear plane displacements and for which there is no longer cohesion of the interface) as a function of the normal stress with a y-intercept forced to zero as shown in Figure 13(b). Indeed, when there is no longer cohesion of the block-mortar interface (i.e., $d = 1$ for the whole interface area), the residual stress is expected to be equal to the effective frictional stress such as $\sigma_{II} = \sigma_\mu = \tilde{\sigma}_{\mu_c} = \mu\sigma_I$. As shown from Fig. 13(b), the friction coefficient of the interface limestone block-lime mortar is estimated to $\mu = 0.81$ and reported in Table 2.

The second parameter which can be directly estimated from the experimental responses plotted in Fig. 13(a) is the initial stiffness K_{II}^0 of the block-mortar interface. The initial stiffness K_{II}^0 is estimated from linear regression of the initial elastic part of the experimental responses and the value obtained is reported in Table 2.

Contrarily to initial stiffness K_{II}^0 and friction coefficient μ, the shear strength σ_{II}^e, the total cohesive energy $G_{f_{II}}$ and the exponent p of the power function $f(d)$ cannot be directly identified from the experimental responses. Latter cohesive and frictional parameters are estimated by matching the experimental responses according to the theoretical behavior expected from FCZM described in Eq.(32). Nevertheless, in the mechanical response of the block-mortar interface, the accurate description of the stress and displacement at

peak load appear relevant while the accuracy of the description of the response as a whole appears less important. Thus, a large quantity of σ^e_{II}, $G_{f_{II}}$ and p combinations are tested and, for each combination, a first normalized square deviation between experimental and numerical peak loads (stress and displacement) are computed and a second one is computed from the whole experimental and numerical responses. On this basis, in order to ensure a description of the peak load with accuracy, a weight of 5/10 is given arbitrarly to the normalized square deviation linked to peak load value and 4/10 is given (arbitrarly) to the one linked to the displacement at peak load (*i.e.* a weight of 9/10 for peak load) while a weight of 1/10 is considered for the normalized square deviation corresponding to the whole response. The fit-

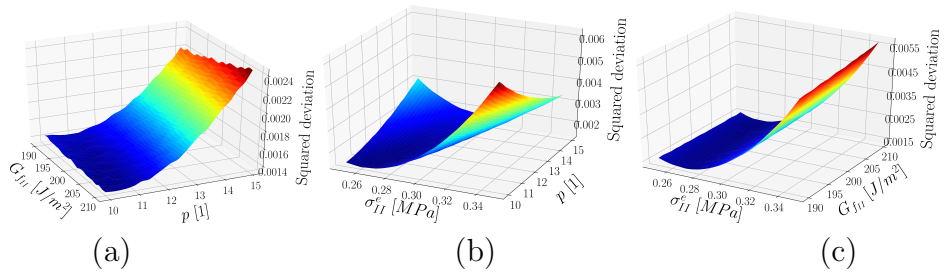

Figure 14: Square deviation evolution for: (a) $\sigma^e_{II} = 0.27$ MPa, (b) $G_{f_{II}} = 206$ J/m^2 and (c) $p = 11$

ting method proposed here leads to a single combination solution as shown in Figure 14 even if Mode II cohesive energy $G_{f_{II}}$ has a lesser impact on the best response compared to shear strength σ^e_{II} and exponent p of the power function $f(d)$. Cohesive parameters and frictional one are reported in Table 2 while the shear stress *vs* shear plane displacement of the block-mortar interface obtained from FCZM [Eq. 32] are plotted as black color curves in Fig. 13(a).

Finally, let us emphasize that the experimental shear stress *vs* shear plane displacement responses of the block-mortar interface are described from FCZM [Eq. 32] with a reasonable accuracy and especially from a single set of cohesive parameters (*i.e.* independent of the normal stress applied on the interface).

Moreover, note that the FCZM model presented here will be able to describe the flattening of the shear stress *vs* shear displacement response usually observed in the case of high normal stress level as shown from Fig.13(a) (or from Fig.10b in D'Altri et al, 2019). Indeed, as it can be deduced from Fig.

13(a), for large critical frictional stress $\sigma_{\mu_c} = \mu\sigma_I$ compared to the interfacial shear strength σ_{II}^e, it is expected that the peaked shape of the response vanishes to the benefit of a response close to the one associated with the frictional stress. In the opposite case, *i.e.* when the normal stress to the interface is weak (Fig.10b in D'Altri et al, 2019), the FCZM proposed here will be able to exhibit the peaked shape of the response because the cohesive stress becomes predominant compared to the frictional one.[3]
Note that the flattening of the shear stress *vs* shear displacement response with respect to the normal stress value (exhibited by the FCZM proposed here) is not reachable by *classical* FCZM (*i.e.* based on the superimposition of the full friction stress and the cohesive one) because, whatever the normal stress is, the difference between the peak stress and the critical frictional stress remains constant and equal to the cohesive shear strength.

The two characterization tests proposed here (direct tensile test on duo and shear test on triplet) are designed to lead to almost uniform loading along the block-mortar interface. In both tests, the damage tends to spread uniformly over the entire surface of the interface and hence allows to estimate the behavior of the assembly block-joint-block and especially the one of the interface block mortar at the mesoscopic scale. If from a theoretical point of view, FCZM can be used at the microscopic scale (local response of the material), the estimate of cohesive and frictional parameters of FCZM obtained from both tests and given in Table 2 is performed at the mesoscopic scale, with the aim of using it on this scale. Note that, the notion of mesoscopic scale is important for the future use of FCZM for masonry simulations and especially in a code based on Discrete Element Method (DEM). Indeed, in the case of large structure sizes simulations, only a few contact points are usually considered on each face of the blocks and hence each contact point is associated with a surface of the block-mortar interface of several tens of square centimeters.

In the following section, the ability of FCZM to describe an experimental cyclic shear loading applied on the triplet specimen is shown and discussed.

[3]The flattening phenomenon experimentally observed on the shear stress *vs* shear displacement response with respect to the normal stress level is at the source of the underestimation of the cohesive behavior (and especially of the cohesive energy) when this one is simply estimated by subtracting the full friction stress from the total shear stress *vs* shear displacement response because the part supposed to correspond to the cohesive behavior decreases with respect to normal stress level.

6. Triplet shear test under unilateral cyclic loading: experimental *vs* numerical responses

In order to use the FCZM in the case of complex loading, the model was implemented in the LMGC90 code (Dubois et al., 2011) based on the Discrete Element Method (DEM) and more specifically on the *Non Smooth Contact Dynamics* (Moreau, 1988; Jean, 1999). As a first attempt, FCZM is used to describe the experimental response obtained from unilateral cyclic shear loading applied on triplet specimen.

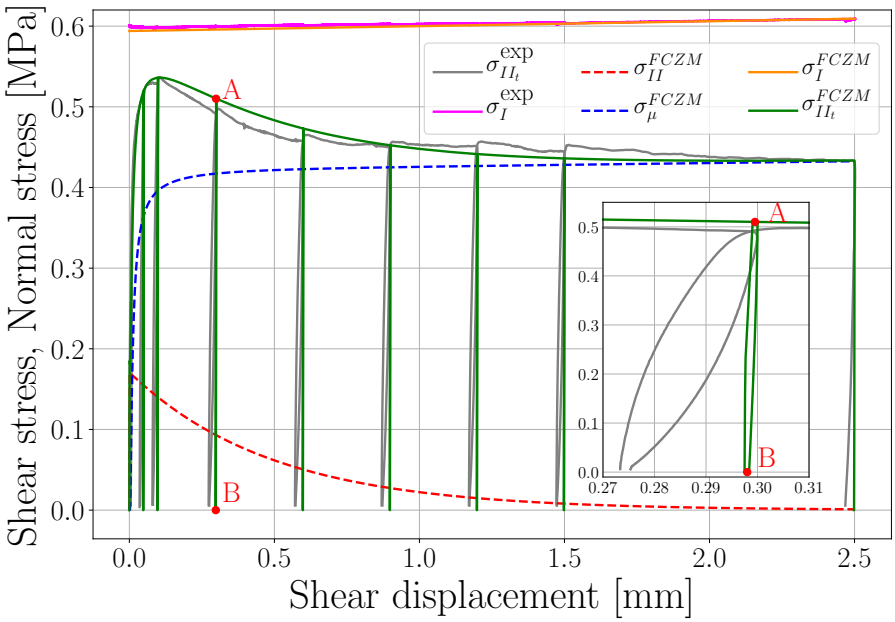

Figure 15: Experimental and simulated shear stress *vs* shear plane displacement response of the joint and block-mortar interface obtained from an unilateral cyclic loading.

Using the same experimental setup as the one described in Section 5.3, a cyclic loading test leads to the typical shear stress *vs* shear plane displacement response plotted in Figure 15. Note that the shear plane displacement corresponds here to the one of the mortar joint and of the block-mortar interface, *i.e.* only the contribution of the limestone is subtracted from the average displacement measured from the four extensometers. The experimental response plotted in Fig.15 is obtained for a normal stress value of 0.6

Designation	Quantity	Symbol	Value	Unit
Mode II	Initial stiffness	K_{II}^0	3.4×10^{11}	Pa/m
	Maximum stress	σ_{II}^e	0.17	MPa
	Cohesive energy	Gf_{II}	83	J/m^2
Frictional parameters	Frictional coefficient	μ	0.71	1
	$f(d)$ function exponent	p	15	1
	Normal stress	σ_I	0.59	MPa

Table 3: FCZM parameters fitted to describe the typical response obtained from the unilateral cyclic shear loading applied on triplet specimen (Fig. 15)

MPa and exhibits jumps of the shear stress associated with each onset of loading and unloading phases as theoretically expected from the discussion proposed in Section 4.2.

A 2D simulation of the unilateral shear test is carried out using LMGC90 software considering rigid blocks and two mortar joints modelled by deformable elements meshed with 25 regular quadrangles in the height and 2 in the width as shown in Fig. 16. Young's modulus of joint elements is $E_j = 3.95$ GPa while Poisson's ratio $\nu = 0.2$. Moreover, the experimental joint failure being mainly interfacial, only the interfaces block-joint associated with the central block are considered, the other two interfaces are coupled at rigid blocks to prevent the relative displacement between ends block and joints. Note that the blocks being modelled from rigid bodies, their geometry is not relevant in this simulation, only the geometry and dimensions of the joints need to correspond to experimental ones. Two contact points per finite element are considered leading to a total of 50 contact points along each interface. The modelling of the unilateral cyclic shear test from LMGC90 code is performed by first applying the normal force to the end blocks and then by loading the central block through the contact of a rigid body (not shown in Fig. 15) on which a vertical velocity-time function reproducing experimental loading cycles is imposed. The shear loading procedure by contact allows to lose contact with the central block and thus to achieve a complete shear unloading of the specimen between two consecutive cycles.

Firstly, FCZM parameters are fitted, according to the procedure described in Section 5.3.2, to describe the envelope of the typical experimental shear stress *vs* shear plane displacement response. The simulated σ_{II_t} *vs* δ_{II} response is plotted in Figure 15 and its envelope appears to be consistent with the experimental one. Note that FCZM parameters obtained to describe the

experimental response are given in Table 3 and differ from those given in Table 2 because they correspond to a given experimental triplet specimen while those given in Tab. 2 result from the fitting procedure applied on a set of triplets (Section 5.3.2).
In a second time, the cyclic loading is simulated and the obtained response is plotted in Fig. 15. As shown from Fig. 15, the onset of experimental loading and unloading phases and associated residual displacements are described by the model with a reasonable accuracy. Let us remember that a

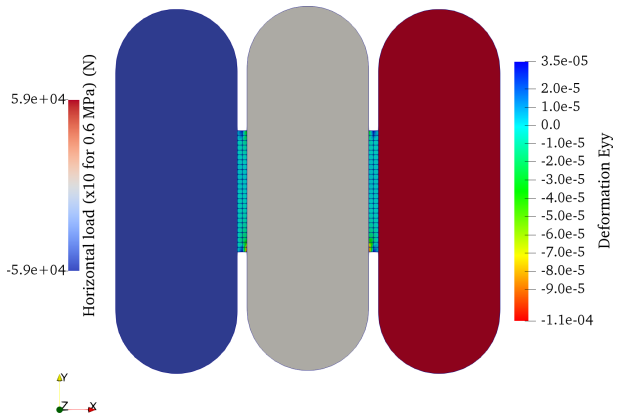

Figure 16: Numerical model of the triplet shear test (LMGC90)

jump of the total shear stress σ_{II_t} associated with a blockage of the interface displacement is expected at the onset of loading and unloading phases when the cohesive stress σ_{II} becomes lesser than the critical frictional one $\sigma_{\mu_c}(d)$ which is the case here for all the loading and unloading phases as shown from the evolutions of cohesive stress and of the critical frictional one plotted in red color and blue color respectively in Fig. 15. Moreover, as shown from the inserted graph in Fig. 15 which corresponds to a zoom of the onset of loading and unloading phases A-B, the experimental and numerical responses are characterized by a slope which correspond to the stiffness of the joint (the interface displacements being mainly blocked during loading-unloading phases). The fact that the experimental stiffness of the joint differs from the numerical one (inserted graph in Fig.15) could be explained by the fact that, experimentally, the damage is not fully located on the interfaces but also diffuses in the mortar joint inducing a decrease of the joint stiffness which is not taken into account in the simulation. Moreover, experimental cycles exhibit more pronounced hysteresis loops than simulated ones which seems to

indicate the existence of dissipative mechanisms other than the only damage and friction at the block-mortar interface. Finally, note that thin hysteresis loops exhibited by the simulation are only due to the fact the contact points along the interfaces do not show the same $(\sigma_{IIt}, \delta_{II})$ state at the same time in the sense that, if the the majority of the contact points are blocking, some of contact points are still sliding.

7. Conclusions

In this paper, a general Frictional Cohesive Zone Model dedicated to quasi-brittle failure is proposed. The model is based on pure Mode I and Mode II cohesive behaviors whose softening part is described from an exponential function and on Coulomb's law for the frictional behavior.

Under combined traction and shear loadings, the coupling between Mode I and Mode II cohesive behaviors is obtained from two criteria (damage initiation criterion and failure criterion) proposed by Camanho et al. (2003). The analytical study of the cohesive energy dissipated as function of loading path emphasizes that proposed FCZM exhibits a load path dependency which is in agreement with the one observed in quasi-brittle fracture.

Under combined compression and shear loadings, taking inspiration of several preceding works which revised the assumption of simple superposition of full friction and Mode II cohesive behavior, a coupling between friction effect and cohesive behavior is proposed through the damage variable (single internal variable of the FCZM). Indeed, the damage variable gives an estimation of the effective damage area of the interface and we assume here that the effective friction phenomenon takes place on part of all of the damage area as a function of the damage level. On this basis, FCZM exhibits a progressive rising friction stress as a function of the shear plane displacement which leads to a smooth transition from a cohesive zone to a pure contact zone.

Applied to the context of masonry, FCZM can be fully characterized from two fracture tests carried out on small masonry assemblages. Mode I cohesive parameters are estimated from a tensile fracture test carried out on duo of limestone blocks assembled by one lime mortar joint while the Mode II cohesive parameters and the frictional ones are estimated from a shear test performed on a triplet of limestone blocks assembled by two lime mortar joints. If the estimation of Mode I cohesive parameters is directly obtained from the tensile stress *vs* interface opening response, the estimation of Mode

II and frictional parameters needs, firstly, the estimate of the friction coefficient from the residual shear stresses with regard to the normal stress imposed on the joint, then, an indirect estimation procedure needs to be used in order to simultaneously determine the Mode II cohesive parameters and the parameter driving the evolution of the friction stress as a function of the damage variable value. The proposed methodology is discussed and it is shown that this one leads to a single set of cohesive and frictional parameters to describe the shear stress *vs* shear plane displacement responses. Moreover, FCZM describes the flattening of the shear stress *vs* shear displacement response as a function of the normal stress value usually observed experimentally. Such a phenomenon is not possible to describe from *classical* FCZM (*i.e.* based on the superimposition of the full friction stress and the cohesive one) because, whatever the normal stress is, the difference between the peak stress and the critical frictional stress remains constant and equal to the cohesive shear strength in these models.

Finally, the FCZM is implemented in LMGC90 discrete element code and is used to simulate the experimental response of an unilateral cyclic shear test carried on a triplet of lime stone assembled by two lime mortar joints. The envelope of a typical shear stress *vs* shear plane displacement response is described by the FCZM with a reasonable accuracy as well as the experimental stress jumps and corresponding residual displacements associated with the onset of the loading and unloading phases.

FCZM will be used shortly to simulate the mechanical behavior of masonry panels submitted to constant vertical load (three vertical load levels) and to a progressive horizontal load up to failure of the panel. Indeed, this kind of loading applied on masonry panels lead to various loading modes as a function of the considered area of the panel (traction, compression, shear, combined traction or compression and shear) and hence simulations of such experiments should constitute a large base of validation of the model.

8. Acknowledgments

The authors thank AIA Ingénierie company (Architectes Ingénieurs Associés) and escially Alain Popinet (Agency Director) and the French National Association of Research and Technology (ANRT) for supporting the study (2016/1369). We also thank Bernard Solbes for his technical expertise in experimental tests. The experimental part of the study has been performed

from the Xyloplate platform equipments - Equipex XYLOFOREST (ANR-10-EQPX-16) - supported by the French National Research Agency (ANR).

References

Abdou, L., Ami Saada, R., Meftah, F., Mebarki. A., 2002. Experimental investigations of the joint-mortar behavior. Mechanics Research Communications 33, 370-384.

Acary, V., Monerie, Y., 2006. Nonsmooth fracture dynamics using a cohesive zone approach. Rapport de Recherche INRIA 6032.

Almeida, J.C., Lourenço, P.B., Baros, J.A., 2002. Characterization of brick and brickmortar interface under uniaxial tension. International Seminar on Structural Masonry for Developing Countries VII, 67–76.

Alfano, G., Sacco, E., 2006. Combining interface damage and friction in a cohesive-zone model, International Journal for Numerical Methods in Engineering 68,542-582.

Baek, H., Park, K., 2018. Cohesive frictional-contact model for dynamic fracture simulations under compression. International Journal of Solids and Structures 144-145, 86–99.

Bisoffi-Sauve, M., Morel, S., Dubois, F., 2019. Modelling mixed mode fracture of mortar joints in masonry buildings. Engineering Structures 182, 316–330.

Bisoffi-Sauve, M., 2016. Etude des ouvrages maonnés en pierre par la méthode des éléments discrets : caractérisation et modélisation du comportement cohésif des joints. PhD Thesis, Université de Bordeaux.

van den Bosch, M.J., Schreurs, P.J.G., Geers, M.G.D., 2006. An improved description of the exponential Xu and Needleman cohesive zone law for mixed-mode decohesion. Engineering Fracture Mechanics 73, 1220–1234.

Camacho, G.T., Ortiz, M., 1996. Computational modelling of impact damage in brittle materials. International Journal of solids and structures 33, 2899–2938.

Camanho, P.P., Davila, C.G., de Moura, M.F., 2003. Numerical simulation of mixed-mode progressive delamination in composite materials. Journal of Composite Materials 37, 14151438.

Chaboche, J.-L., Girard, R., Schaff, A., 1997. Numerical analysis of composite systems by using interphase/interface models. Computational Mechanics 20, 3–11.

D'Altri, A.M., de Miranda, S., Castellazzi, G., Sarhosis V., 2018. A 3D detailed micro-model for the in-plane and out-of-plane numerical analysis of masonry panels. Computers and Structures 206, 18–30.

D'Altri, A.M., Messali, F., Rots, J., Castellazzi, G., de Miranda, S., 2019. A damaging block-based model for the analysis of the cyclic behaviour of full-scale masonry structures. Engineering Fracture Mechanics 209, 423–448.

Dimitri, R., Trullo, M., De Lorenzis, L., Zavarise, G., 2015. Coupled cohesive zone models for mixed-mode fracture: A comparative study. Engineering Fracture Mechanics 148, 145–179.

Dubois, F., Jean, M., Renouf, M., Mozul, R., Martin, A., Bagnéris, M., 2011. LMGC90. 11ème Colloque National en Calcul des Structures, Giens, France.

EN 1015-11, 2007. Methods of test for mortar for masonry - Part 11: Determination of flexural and compressive strength of hardened mortar. AFNOR.

EN 1052-3, 2007. Methods of test for masonry - Part 3: Determination of initial shear strength. AFNOR.

EN 1926, 2006. Natural stone test methods - Determination of uniaxial compressive strength. AFNOR.

EN 13733, 2002. Products and systems for the protection and repair of concrete structures - Test methods - Determination of the durability of structural bonding agent . AFNOR.

Freddi, F., Sacco, E., Serpieri, R., 2017. An enriched damage-frictional cohesive-zone model incorporating stress multi-axiality. Meccanica, 1–20.

Hillerborg, A., Modéer, M., Petersson, P.-E., 1976. Analysis of crack formation and crack growth in concrete by means of fracture mechanics and finite elements. Cement and concrete research 6, 773–781.

Högberg, J. L., 2006. Mixed mode cohesive law. International Journal of Fracture 141, 549–559.

Jean, M., 1999. The non-smooth contact dynamics method. Computer Methods in Applied Mechanics and Engineering 177, 235–257.

Lourenço, P.B., Ramos, L.F., 2004. Characterization of cyclic behavior of dry masonry joints. Journal of Structural Engineering 130, 779–786.

van Mier, J.G.M., 1996. Fracture Processes of Concrete. CRC Press.

Moreau, J.J., 1988. Unilateral contact and dry friction in finite freedom dynamics. Nonsmooth mechanics and Applications, Vienna: Springer, 1–82.

Morel, S., Lespine, C., Coureau, J.-L., Planas, J., Dourado, N., 2010. Bilinear softening parameters and equivalent LEFM R-curve in quasibrittle failure. International Journal of Solids and Structures 47, 837–850.

van der Pluijm, R., 1993. Shear behavior of bed joints. Proceedings of 6th North American masonry conference, 125–136.

van der Pluijm, R., 1999. Out-of-plane bending of masonry: behavior and strength. PhD Thesis, Technische Universiteit Eindhoven.

Raous, M., Monerie, Y., 2002. Unilateral contact, friction and adhesion: 3D cracks in composite materials, 3rd Contact Mechanics. International Symposium, Contact Mechanics, J.A.C. Martins and M.D.P. Marques (Eds), 333–346.

Sandoval, C., Arnau, O., 2017. Experimental characterization and detailed micro-modeling of multi-perforated clay brick masonry structural response. Materials and Structures 50, 34.

Snozzi, L., Molinari, J-F., 2013. A cohesive element model for mixed mode loading with frictional contact capability. International Journal for Numerical Methods in Engineering 93, 510–526.

Spring, D.W., Paulino, G.H., 2015. Computational homogenization of the debonding of particle reinforced composites: The role of interphases in interfaces. Computational Materials Science 109, 209–224.

Xu, X.-P., Needleman, A., 1993. Void nucleation by inclusion debonding in a crystal matrix. Modelling and Simulation in Materials Science and Engineering 1, 111-132.

Yuen, T.Y.P., Deb, T., Zhang, H., Liu, Y., 2019. A fracture energy based damage-plasticity interfacial constitutive law for discrete finite element modelling of masonry structures. Computers and Structures 220, 92–113.

Zhang, S., Taheri Mousavi, S.M., Richart, N., Molinari, J.-F., Beyer, K., 2017. Micro-mechanical finite element modeling of diagonal compression test for historical stone masonry structure. International Journal of Solids and Structures 112, 122–132.

Zhang, J., Liang, N.-G., Deng, S.-C., Liu, J.-X., Liu, X.-Y., Fu, Q., 2008. Study of the Damage-induced Anisotropy of Quasi-brittle Materials using the Component Assembling Model. International Journal of Damage Mechanics 17, 197–221.

Zimmermann, T., Strauss, A., Bergmeister, K., 2005. Structural behavior of low- and normal-strength interface mortar of masonry. Materials and Structures 45, 829–839.

Zucchini, A., Lourenço, P.B., 2002. A micro-mechanical model for the homogenisation of masonry. International Journal of Solids and Structures 39, 3233–3255.